

# Orbital Optical Raman Lattice

Zhi-Hao Huang,<sup>1,2,\*</sup> Kou-Han Ma,<sup>1,2,\*</sup> Bao-Zong Wang,<sup>1,2</sup> W. Vincent Liu,<sup>3,4</sup> and Xiong-Jun Liu<sup>1,2,4,†</sup>

<sup>1</sup>*International Center for Quantum Materials and School of Physics, Peking University, Beijing 100871, China*

<sup>2</sup>*Hefei National Laboratory, Hefei 230088, China*

<sup>3</sup>*Department of Physics and Astronomy and IQ Initiative,  
University of Pittsburgh, Pittsburgh, PA 15260, USA*

<sup>4</sup>*International Quantum Academy, Shenzhen 518048, China*

The spin and orbital are two basic degrees of freedom, which play significant roles in exploring exotic quantum phases in optical lattices with synthetic spin-orbit coupling (SOC) and high orbital bands, respectively. Here, we propose an orbital optical Raman lattice to study exotic high-orbital Bose condensates with Raman-induced SOC in a square lattice. We find that both the SOC and  $p$ -orbital interactions influence the condensed state of bosons. Their interplay results in two novel high-orbital many-body quantum phases: the uniform angular momentum superfluid phase, which features a global topological chiral orbital current, and the two-dimensional spin-orbital supersolid phase, which is characterized by the spin and orbital angular momentum density wave patterns. The former has topological Bogoliubov excitations characterized by a uniform Chern number, while the spin-orbital supersolid phase hosts topological excitations with opposite Chern numbers which respectively protect the chiral and antichiral edge modes in the neighboring supersolid clusters. Our findings may inspire a new avenue for exploring exotic SOC and high-orbital physics in optical lattices, and shall also advance the experimental progress of novel supersolids in higher dimensions.

*Introduction.* Ultracold atomic gases provide ideal platforms for quantum simulation due to their pristine nature and full controllability [1, 2]. Among them, investigations into synthetic gauge fields [3–11] and spin-orbit couplings (SOCs) [12–28] have attracted widespread interests. Over the past decade, experimental realizations of novel SOC in one-dimension [14, 17, 18, 24–26], two-dimension [23, 29–32], and three-dimension [33] have enabled the simulation of various exotic topological models with cold atoms, such as topological semimetals [33], quantum anomalous Hall insulator [34], and non-Hermitian topological phases [35]. Additionally, extending synthetic SOC to strongly correlated regime facilitates the realization of non-Abelian dynamical gauge fields [36]. Besides simulating topological quantum phases [37–43], the quest for supersolids characterized by diagonal and off-diagonal long-range order in ultracold atoms has never ceased [44–46]. Currently, the supersolid phase has been observed in long-range interacting dipolar quantum gases [47–53] and optical cavities [54, 55].

High-orbital (e.g.  $p$  and  $d$ ) systems in optical lattices also received considerable attention due to their rich degrees of freedom, which can give rise to exotic orbital physics [56–63]. With the orbital degree of freedom, one can not only simulate the behavior of electrons in realistic materials but also, more crucially, uncover new concepts and phenomena that have no prior analog in electronic systems [63], such as the high-orbital Bose-Einstein condensates (BECs) with novel orbital ordering [64–79]. To date, significant progresses have been made in the study of  $p$ -orbital BEC in optical lattices. For instance, the  $p$ -orbital BEC in a square lattice manifests as a superfluid phase with a staggered angular momentum order that breaks time-reversal symmetry [66]. In a triangular lattice, it results in staggered loop current orders [67, 79],

and in a hexagonal lattice, it exhibits Potts-nematic superfluid order [76] or atomic chiral superfluidity with topological Bogoliubov excitations [77]. Such phases reveal the remarkable richness of higher orbital coherence whether or not breaking the time-reversal symmetry.

In this letter, we propose an orbital optical Raman lattice that combines the both topics of synthetic SOC [21, 23, 28] and  $p$ -orbital condensates [66] in a square lattice, and predict two novel quantum many-body phases with nontrivial topology: the uniform angular momentum superfluid (UAMSF) and the 2D spin-orbital supersolid (SOSS), as characterized by different spin and orbital angular momentum orders. The condensed state of bosons is shown to be governed by the nontrivial interplay effects of the on-site  $p$ -orbital interactions and Raman-induced SOC. For the  $p$ -orbital interaction dominating over the Raman-induced SOC, the ground state exhibits a uniform angular momentum order, dubbed the UAMSF, which hosts uniform chiral topological excitations. In contrast, when the  $p$ -orbital interaction is comparable to SOC, the staggered spin and angular momentum cluster patterns emerge, leading to the 2D topological SOSS which host chiral and antichiral topological edge excitations in the neighboring supersolid clusters. Our work offers a new perspective for exploring exotic high-orbital physics with nontrivial SOC effects and shall advance the realization of novel supersolid phases without long-range interactions in ultracold atom systems.

*Model.* We start with the Hamiltonian for ultracold bosons trapped in an orbital optical Raman lattice, given by  $H_0 = \frac{p_x^2}{2m} + \frac{p_y^2}{2m} + V(x, y) + M(x, y)\sigma_x + m_z\sigma_z$ . Here,  $V(x, y) = -V_0[\cos^2(\frac{\pi}{a}x) + \cos^2(\frac{\pi}{a}y)]$  and  $M(x, y) = -M_0[\cos(\frac{\pi}{a}x) + \cos(\frac{\pi}{a}y)]$  represent the normal lattice potential and Raman field, respectively. The Pauli matrices

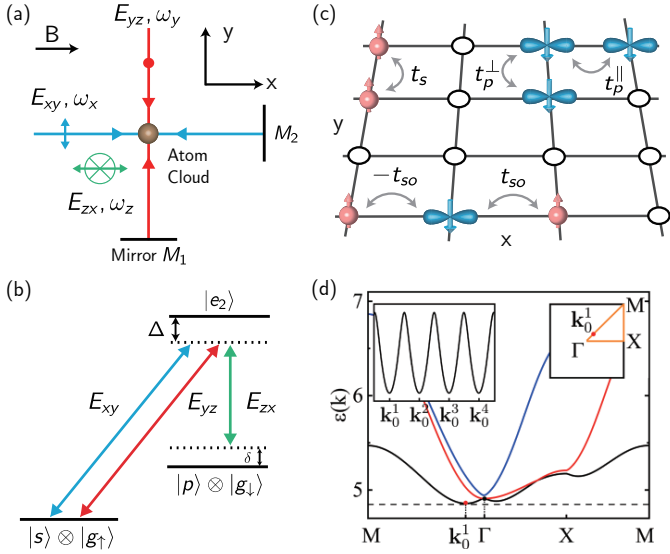


FIG. 1. (a) Generic setup for orbital optical Raman lattice. The bias magnetic field  $\mathbf{B}$  is parallel to the  $x$  direction. A pair of standing waves,  $\mathbf{E}_{xy}$  and  $\mathbf{E}_{yz}$ , produce a square lattice. Moreover, the Raman field can be achieved by applying another plane wave  $\mathbf{E}_{zx}$ . (b) Optical-dipole transition diagram for Raman coupling in cold bosons ( $^{87}\text{Rb}$ ) coupled to two pairs of laser beams ( $\mathbf{E}_{xy}$ ,  $\mathbf{E}_{zx}$ ) and ( $\mathbf{E}_{yz}$ ,  $\mathbf{E}_{zx}$ ). Here the hyperfine states  $|1, -1\rangle$  and  $|1, 0\rangle$  of  $^{87}\text{Rb}$  are used to emulate the ground states  $|g_{\uparrow, \downarrow}\rangle$ . (c) The sketch for the nearest-neighbor spin-conserved hopping for  $s$  and  $p_{x,y}$  orbitals and the spin-flipped hopping between  $s$  and  $p_{x,y}$ . Here, Only the  $p_x$  orbital is displayed, since the hopping terms for  $p_x$  and  $p_y$  are related by  $C_4$  symmetry. (d) Single-particle spectrum.  $\mathbf{k}_0^1$ ,  $\mathbf{k}_0^2$ ,  $\mathbf{k}_0^3$ ,  $\mathbf{k}_0^4$  are the lowest energy points connected by  $C_4$  symmetry. Thereinafter,  $V_0 = 5.0E_r$ ,  $M_0 = 1.0E_r$  (tight-binding parameters:  $t_s = 0.0658E_r$ ,  $t_p^{\parallel} = 0.4228E_r$ ,  $t_p^{\perp} = 0.0658E_r$ ,  $t_{so} = 0.1059E_r$ ,  $\mu_s = 5.1909E_r$ , and  $\mu_p = 5.9049E_r$ ),  $m_z = 0.0173E_r$ . Besides,  $\mathbf{k}_0^1 = (0.154, 0.154)\pi$ . Note that  $E_r$  is the recoil energy.

ces  $\sigma$  act on the subspace spanned by  $|s\rangle \otimes |g_{\uparrow}\rangle$  and  $|p\rangle \otimes |g_{\downarrow}\rangle$ , where the spin  $|g_{\uparrow, \downarrow}\rangle$  is defined from hyperfine ground states,  $|s\rangle$  and  $|p\rangle$  represent local orbital states. The model Hamiltonian  $H_0$  can be realized with high feasibility, through the three-laser configuration shown in Fig. 1(a). Two lasers form standing waves,  $\mathbf{E}_{xy} = \hat{y}E_0 \cos(k_0x)$  and  $\mathbf{E}_{yz} = \hat{z}E_0 \cos(k_0y)$ , linearly polarized along  $y$  and  $z$  axes, respectively, and propagating in  $x$ - $y$  plane. The third laser forms a plane wave,  $\mathbf{E}_{zx} = \hat{x}E_z e^{-ik_z z}$  propagating along  $z$  direction and is  $x$ -polarized. The standing waves  $\mathbf{E}_{xy}$  and  $\mathbf{E}_{yz}$  coupling to excited states with a red detuning  $\Delta$  contribute to the diagonal square optical lattice potentials  $V(x, y) = \hbar(|\mathbf{E}_{xy}|^2/\Delta + |\mathbf{E}_{yz}|^2/\Delta)$ . Additionally,  $\mathbf{E}_{xy}$ ,  $\mathbf{E}_{yz}$ , and  $\mathbf{E}_{zx}$  induce the Raman field components  $M(x)$  and  $M(y)$  via two two-photon transitions as illustrated in a  $\Lambda$ -type configuration [Fig.1(b)]. In experiment one can easily set that the Raman field only couples  $|s\rangle \otimes |g_{\uparrow}\rangle$  and  $|p\rangle \otimes |g_{\downarrow}\rangle$  by putting such two states be nearly reso-

nant for the two-photon transitions except for a tunable two-photon detuning  $\delta$ , which defines an effective Zeeman splitting  $m_z = \hbar\delta/2$ , while all other orbital states are far detuned [80].

With the above implementation scheme, bosons can occupy the spin-orbital locking states  $\phi_{s\uparrow}$ ,  $\phi_{p_{x\downarrow}}$ , and  $\phi_{p_{y\downarrow}}$ . As shown in Fig.1(c), the lattice potential  $V(x, y)$  governs spin-conserved nearest-neighbour hopping ( $t_s$  and  $t_p$ ), while the Raman field  $M(x, y)$  contributes to spin-flipped nearest-neighbour hopping ( $t_{so}$ ). Since the Raman field  $M(x, y)$  has twice the period of the optical lattice  $V(x, y)$  and is symmetric with respect to each lattice site center of  $V(x, y)$ , the spin-flipped hopping is staggered in the  $\nu$  ( $\nu = x, y$ ) direction with  $t_{so}^{(i, i \pm e_{\nu})} = \pm(-1)^{i_{\nu}} t_{so}$  [80]. The staggered factor  $(-1)^{i_{\nu}}$  represents a nontrivial momentum transfer between spin-up and spin-down states in the Raman coupling, and can be absorbed by the transformation  $b_{i, \nu, \downarrow} \rightarrow -(-1)^{i_{\nu}} b_{i, \nu, \downarrow}$ , yielding the tight-binding Hamiltonian

$$\begin{aligned} \hat{H}_0 = & (\mu_s + m_z) \sum_{\mathbf{i}} n_{\mathbf{i}, s, \uparrow} + (\mu_p - m_z) \sum_{\mathbf{i}, \nu} n_{\mathbf{i}, \nu, \downarrow} \\ & - t_s \sum_{\langle \mathbf{i}, \mathbf{j} \rangle} b_{\mathbf{i}, s, \uparrow}^{\dagger} b_{\mathbf{j}, s, \uparrow} - \sum_{\mathbf{i}, \mu, \nu} (\bar{t}_p^{\mu\nu} b_{\mathbf{i}, \mu, \downarrow}^{\dagger} b_{\mathbf{i} + \mathbf{e}_{\nu}, \nu, \downarrow} + \text{H.c.}) \\ & + t_{so} \sum_{\mathbf{i}, \nu} \sum_{\delta_{\nu} = \pm \mathbf{e}_{\nu}} [\text{sgn}(\delta_{\nu}) b_{\mathbf{i}, \nu, \downarrow}^{\dagger} b_{\mathbf{i} + \delta_{\nu}, s, \uparrow} + \text{H.c.}], \quad (1) \end{aligned}$$

where  $b_{\mathbf{i}, l, \sigma}^{\dagger}$  ( $b_{\mathbf{i}, l, \sigma}$ ) ( $l = s, p_x, p_y$ ) denotes the creation (annihilation) operator of boson.  $\bar{t}_p^{\mu\nu} = t_p^{\parallel} \delta_{\mu\nu} + t_p^{\perp} (1 - \delta_{\mu\nu})$  ( $\mu, \nu = x, y$ ),  $n_{\mathbf{i}, l, \sigma} = b_{\mathbf{i}, l, \sigma}^{\dagger} b_{\mathbf{i}, l, \sigma}$ , and  $\mu_{s, p}$  denote the on-site energies. A key feature is that the momentum transfer by Raman field forces the band minima of  $\epsilon_{p_{x\downarrow}}(\mathbf{k})$  ( $\epsilon_{p_{y\downarrow}}(\mathbf{k})$ ) to move from  $\mathbf{Q}_x = (\pi, 0)$  ( $\mathbf{Q}_y = (0, \pi)$ ) to  $\Gamma$  [80]. Further, the remaining 2D SOC effect can result in a single-particle spectrum with four  $C_4$ -connected minima at  $\mathbf{k}_0^1$ ,  $\mathbf{k}_0^2$ ,  $\mathbf{k}_0^3$ , and  $\mathbf{k}_0^4$  [Fig.1(d)], leading to the major novel physics predicted in the present orbital optical Raman lattice. A quadratic band touch point protected by time-reversal symmetry exists at  $\Gamma$  [81].

The total Hamiltonian includes also the contact interaction  $V(\mathbf{r} - \mathbf{r}') = g_{\sigma\sigma'} \delta(\mathbf{r} - \mathbf{r}')$  ( $\sigma, \sigma' = \uparrow, \downarrow$ ), whose form in the lattice model reads [80]

$$\begin{aligned} \hat{H}_{\text{int}} = & \sum_{\mathbf{i}} \left[ \frac{U_s}{2} n_{\mathbf{i}, s, \uparrow} (n_{\mathbf{i}, s, \uparrow} - 1) + U_{sp} n_{\mathbf{i}, s, \uparrow} \sum_{\nu} n_{\mathbf{i}, \nu, \downarrow} \right. \\ & + \frac{U_p}{2} \sum_{\nu} n_{\mathbf{i}, \nu, \downarrow} (n_{\mathbf{i}, \nu, \downarrow} - 1) + 2\tilde{U}_p n_{\mathbf{i}, p_x, \downarrow} n_{\mathbf{i}, p_y, \downarrow} \\ & \left. + \frac{\tilde{U}_p}{2} (b_{\mathbf{i}, p_x, \downarrow}^{\dagger} b_{\mathbf{i}, p_x, \downarrow}^{\dagger} b_{\mathbf{i}, p_y, \downarrow} b_{\mathbf{i}, p_y, \downarrow} + \text{H.c.}) \right], \quad (2) \end{aligned}$$

where  $U_s = g_{\uparrow\uparrow} \int d\mathbf{r} |\phi_{s, \uparrow}(\mathbf{r} - \mathbf{r}_i)|^4$ , and the coefficients  $U_{sp}$ ,  $U_p$ , and  $\tilde{U}_p$  can also be similarly defined with  $g_{\sigma\sigma'} \approx g$ . Note that  $U_p$  refers to the intra-orbital interaction for

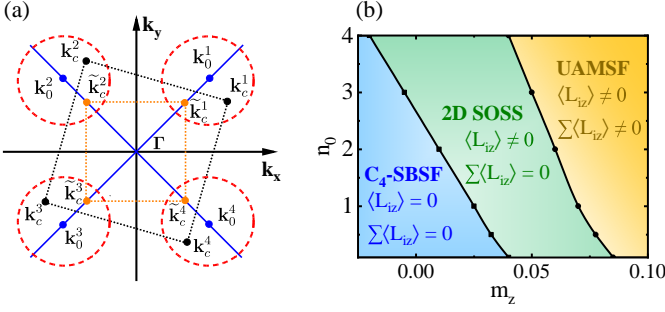


FIG. 2. (a) Schematic of the variational calculation. Here,  $\mathbf{k}_0^n$ ,  $\mathbf{k}_c^n$ , and  $\tilde{\mathbf{k}}_c^n$  ( $n = 1 \sim 4$ ) represent the energy minima of the single-particle spectrum, the variational condensation momenta under weak interaction, and the real condensation momenta, respectively. (b) Ground state phase diagram. Here,  $m_z$  and  $n_0$  denote the effective Zeeman splitting and boson condensation density, respectively. There are three types of ground states:  $C_4$ -symmetry-broken superfluid phase ( $C_4$ -SBSF), two-dimensional spin-orbital supersolid phase (2D SOSS), and uniform angular momentum superfluid phase (UAMSF). Parameters:  $V_0 = 5.0E_r$ ,  $M_0 = 1.0E_r$ , and  $g = 0.01E_r$  ( $U_s = 0.1044E_r$ ,  $U_{sp} = 0.0428E_r$ ,  $U_p = 0.0618E_r$ , and  $\tilde{U}_p = 0.0175E_r$ ).

the  $p_{\nu\downarrow}$  ( $\nu = x, y$ ) orbitals, while  $\tilde{U}_p$  refers to the inter-orbital interaction between the  $p_{x\downarrow}$  and  $p_{y\downarrow}$  orbitals.

*Ground state ansatz and phase diagram.* Usually, the non-interacting BEC will take place at the single-particle band minimum points  $\mathbf{k}_0^n$  ( $n = 1 \sim 4$ ). However, since these lowest energy points of Hamiltonian  $\hat{H}_0$  do not generally correspond to the energy minima of the total Hamiltonian  $\hat{H}_0 + \hat{H}_{\text{int}}$ , the interaction changes the populations in the  $s_{\uparrow}$ ,  $p_{x\downarrow}$ , and  $p_{y\downarrow}$  orbitals, which shifts the condensation momenta around  $\mathbf{k}_0^n$  ( $n = 1 \sim 4$ ). Under weak interaction, the condensed ground state ansatz can be given by  $|g\rangle \sim e^{\sqrt{N_0}b^\dagger}|\text{vac}\rangle$ , where  $b^\dagger$ , expressed as  $b^\dagger = \sum_{n=1}^4 \sum_{l_\sigma} \gamma_{\mathbf{k}_c^n} \beta_{\mathbf{k}_c^n, l_\sigma} b_{\mathbf{k}_c^n, l_\sigma}^\dagger$  ( $l_\sigma = s_{\uparrow}, p_{x\downarrow}, p_{y\downarrow}$ ), represents the quasi-particle creation operator and  $N_0$  is the particle number of BEC. Here,  $C_4$ -related points  $\mathbf{k}_c^n$  [Fig.2(a)] denote the variational condensation momentum, with the variational parameters  $\gamma_{\mathbf{k}_c^n}$  and  $\beta_{\mathbf{k}_c^n}$  satisfying  $\sum_n |\gamma_{\mathbf{k}_c^n}|^2 = 1$  and  $\sum_{l_\sigma} |\beta_{\mathbf{k}_c^n, l_\sigma}|^2 = 1$ , respectively. Note that  $|\gamma_{\mathbf{k}_c^n}|^2$  represents the condensation distribution probability of bosons at  $\mathbf{k}_c^n$ , and  $|\beta_{\mathbf{k}_c^n, l_\sigma}|^2$  denotes the orbital population probability. To identify the true condensation momenta  $\tilde{\mathbf{k}}_c^n$  and the condensation parameters  $(\gamma_{\tilde{\mathbf{k}}_c^n}, \beta_{\tilde{\mathbf{k}}_c^n, l_\sigma})$ , we search for the minimum of the energy density functional  $\langle g | \hat{\mathcal{H}}_0 + \hat{\mathcal{H}}_{\text{int}} | g \rangle / N$  by simulated annealing algorithm [82], where  $N$  is the number of lattice sites. As depicted in Fig.2(a),  $\tilde{\mathbf{k}}_c^n$  ( $n = 1 \sim 4$ ) lie on the diagonal lines and move toward  $\Gamma$  (or coincide with it), and they are also connected by  $C_4$  symmetry.

Here, the nontrivial interplay between the  $p$ -orbital interaction in Eq.(2) and the 2D SOC leads to the emergence of exotic orbital orders with distinct novel topol-

ogy in the condensate state  $|G\rangle$ . The  $p$ -orbital interaction in the present orbital optical Raman lattice tends to generate uniform non-zero orbital angular momentum (OAM) order  $\langle G | L_{i,z} | G \rangle$  ( $L_{i,z} = -ib_{i,p_{x,\downarrow}}^\dagger b_{i,p_{y,\downarrow}} + \text{H.c.}$ ) [66, 80] to reduce the interaction energy, leading to  $\beta_{\tilde{\mathbf{k}}_c^n, p_{x\downarrow}} = \pm i \beta_{\tilde{\mathbf{k}}_c^n, p_{y\downarrow}}$ . However, the Raman-induced SOC in Eq.(1) prefers  $\beta_{\tilde{\mathbf{k}}_c^n, p_{x\downarrow}} = \pm \beta_{\tilde{\mathbf{k}}_c^n, p_{y\downarrow}}$ , suppressing the uniform OAM  $\langle L_{i,z} \rangle$ . Thus, it is this competitive relationship between them that gives rise to three distinct phases: (1) When the SOC dominates over the  $p$ -orbital interaction, the condensate will occur at one of the  $\tilde{\mathbf{k}}_c^n$  ( $n = 1 \sim 4$ ) with  $\beta_{\tilde{\mathbf{k}}_c^n, p_{x\downarrow}} = \pm \beta_{\tilde{\mathbf{k}}_c^n, p_{y\downarrow}}$ , resulting in a  $C_4$ -symmetry-broken superfluid phase without OAM order; (2) In contrast, if the  $p$ -orbital interaction plays the leading role, the bosons condense at the  $\Gamma$  point with  $\beta_{\Gamma, p_{x\downarrow}} = -i \beta_{\Gamma, p_{y\downarrow}}$ , and the condensate exhibits uniform OAM order; (3) Importantly, in the intermediate regime, where the  $p$ -orbital interaction and SOC are comparably strong, the bosons condense equally at the  $\tilde{\mathbf{k}}_c^n$  ( $n = 1 \sim 4$ ), with the orbital parameters given by  $\beta_{\tilde{\mathbf{k}}_c^n, p_{x\downarrow}} = -(-1)^n \beta_{\tilde{\mathbf{k}}_c^n, p_{y\downarrow}}$ , causing a novel OAM density-wave pattern known as the SOSS phase. Fig.2(b) shows the phase diagram plotted versus condensate density  $n_0$  and  $m_z$ , which govern the  $p$ -orbital interaction. A most important feature of the phases in (2) and (3) [orange and green areas in Fig.2(b)] is that they host different types of topological quasiparticles, whose emergence necessitates both the  $p$ -orbital interaction and the Raman induced 2D SOC. We examine them below in detail.

*Uniform angular momentum superfluid.* Adjust the Zeeman splitting  $m_z$  such that onsite energy  $\epsilon_{p\downarrow}(\Gamma)$  is well below  $\epsilon_{s\uparrow}(\Gamma)$ . With the dominant  $p$ -orbital population, the  $p$ -orbital interaction governs the ground state. Consequently, bosons condense at the  $\Gamma$  with orbital parameters  $\beta_{\Gamma, s_{\uparrow}} = 0$  and  $\beta_{\Gamma, p_{x\downarrow}} = -i \beta_{\Gamma, p_{y\downarrow}}$ . As shown in Fig.3(a), this ground state exhibits a uniform OAM order  $\langle L_{i,z} \rangle = 2n_0 |\beta_{\Gamma, p_{y\downarrow}}|^2$  in real space, rendering the UAMSF which breaks time-reversal symmetry. While the ground state is dominated by  $p$ -wave interaction, the quasiparticle excitations are actually governed by both the  $p$ -wave

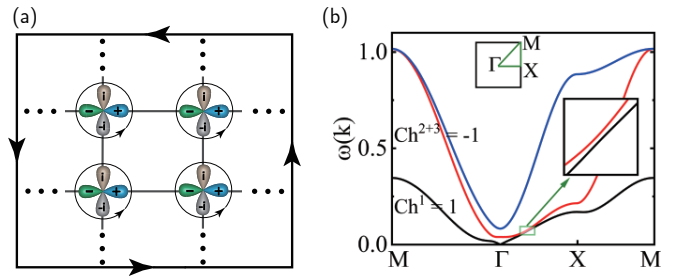


FIG. 3. (a) OAM order  $\langle L_{i,z} \rangle$  and (b) topological quasiparticle excitation spectrum for UAMSF. The parameters:  $m_z = 0.08E_r$ ,  $n_0 = 2.0$ . Other parameters are taken as the same as those in Fig.2.

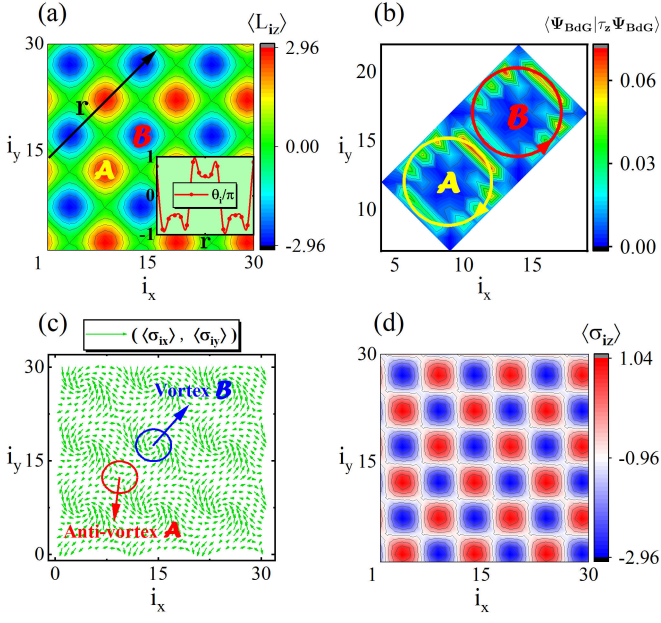


FIG. 4. (a) Spatial distribution of  $\langle L_{i,z} \rangle$  for 2D SOSS phase. The positive ( $\langle L_{i,z} \rangle > 0$ ) and negative ( $\langle L_{i,z} \rangle < 0$ ) OAM clusters are staggered, with  $\sum_{\text{Global}} \langle L_{i,z} \rangle = 0$ . Inset: the relative phase difference  $\theta_i = \text{Im}[\ln \langle b_{i,p_x,\downarrow}^\dagger b_{i,p_y,\downarrow} \rangle]$  between the  $p_x$  and  $p_y$  orbitals along path  $\mathbf{r}$ . (b) Topological edge excitations of the positive A and negative B clusters. The arrows represent the flow directions of the edge currents. (c) Spin field  $(\langle \sigma_{i,x} \rangle, \langle \sigma_{i,y} \rangle)$  displays a topological pattern (skyrmion). (d) Spin component  $\langle \sigma_{i,z} \rangle$  presents another staggered high and low-density clusters pattern. Here, parameters are set as  $m_z = 0.06E_r$ ,  $n_0 = 2.0$ . And the condensation momenta are  $\tilde{\mathbf{k}}_c^1 = (k_c, k_c)$ ,  $\tilde{\mathbf{k}}_c^2 = (-k_c, k_c)$ ,  $\tilde{\mathbf{k}}_c^3 = (-k_c, -k_c)$ , and  $\tilde{\mathbf{k}}_c^4 = (k_c, -k_c)$ . Note that  $k_c = \pi/10$ .

interaction and the 2D SOC, and exhibit nontrivial topology characterized by Chern numbers.

In order to obtain the quasiparticle excitation spectrum, here we employ the Bogoliubov theory to derive the Bogoliubov-de Gennes (BdG) Hamiltonian  $\hat{\mathcal{H}}_{\text{BdG}} = \frac{1}{2} \sum_{\mathbf{k}} \Psi_{\mathbf{k}}^\dagger \mathcal{H}_{\text{BdG}} \Psi_{\mathbf{k}}$  [80], where  $\Psi_{\mathbf{k}}^\dagger = (b_{\Gamma+\mathbf{k},l,\sigma}^\dagger, b_{\Gamma-\mathbf{k},l,\sigma})$  denotes the Nambu basis. Performing the Bogoliubov transformation, we have  $T_{\mathbf{k}}^\dagger \mathcal{H}_{\text{BdG}}(\mathbf{k}) T_{\mathbf{k}} = E_{\mathbf{k}}$ . Here unitary matrix  $T_{\mathbf{k}}$  satisfies  $T_{\mathbf{k}}^\dagger \tau_z T_{\mathbf{k}} = \tau_z$  ( $\tau_z = \sigma_z \otimes \mathbf{I}_{3 \times 3}$ ) and the diagonal terms of  $E_{\mathbf{k}}$  represent the excitation spectrum [83]. As shown in Fig.3 (b), an interaction-induced topological gap opens at the  $\Gamma$  point [81] and, together with the 2D SOC, separates the first band from the second and third bands, leading to the Chern number of the first band  $\text{Ch}^1 = 1$ , while the total topological number of the second and third bands  $\text{Ch}^{2+3} = -1$ . Consequently, these topological excitations are chiral.

*Two-dimensional spin-orbital supersolid.* In the intermediate regime with moderate  $m_z$ , the  $p$ -orbital interaction and the Raman-induced SOC are competitive, and lead to an equal condensation at momenta  $\tilde{\mathbf{k}}_c^n$

( $n = 1 \sim 4$ ) with the condensation parameters satisfying  $|\gamma_{\tilde{\mathbf{k}}_c^n}|^2 = \frac{1}{4}$  and  $\beta_{\tilde{\mathbf{k}}_c^n, p_{x,\downarrow}} = -(-1)^n \beta_{\tilde{\mathbf{k}}_c^n, p_{y,\downarrow}}$ . Here the corresponding OAM order, which is given by  $\langle L_{i,z} \rangle = 2n_0 \sum_{n,n'=1}^4 \text{Im}[e^{-i(\tilde{\mathbf{k}}_c^n - \tilde{\mathbf{k}}_c^{n'}) \cdot \mathbf{i}} \gamma_{\tilde{\mathbf{k}}_c^n}^* \beta_{\tilde{\mathbf{k}}_c^n, p_{x,\downarrow}}^* \gamma_{\tilde{\mathbf{k}}_c^{n'}} \beta_{\tilde{\mathbf{k}}_c^{n'}, p_{y,\downarrow}}]$ , exhibits a staggered positive and negative clusters distribution shown in Fig.4(a), with the periods of the two types of clusters  $\pi/k_c$  in  $x$  and  $y$  directions. The staggered clusters pattern satisfies  $\sum_{\text{Cluster}} \langle L_{i,z} \rangle \neq 0$  but  $\sum_{\text{Global}} \langle L_{i,z} \rangle = 0$ , which means that the time-reversal symmetry is broken within each cluster but recovered by averaging for the global system. The supersolid phase exhibits nontrivial topology at each OAM cluster, as characterized by the chiral and anti-chiral edge states of topological excitations on the boundaries of the OAM clusters A ( $\langle L_{i,z} \rangle > 0$ ) and B ( $\langle L_{i,z} \rangle < 0$ ), respectively [see Fig.4(b)] [80]. The chiral and anti-chiral edge states are protected by the opposite Chern numbers of the bulk topological excitations in the A and B clusters, and they are robust under impurities or disorders.

The present supersolid phase embodies rich and exotic features beyond the OAM order. In particular, we investigate the real-space spin texture  $\langle \sigma_i \rangle = (\langle \sigma_{i,x} \rangle, \langle \sigma_{i,y} \rangle, \langle \sigma_{i,z} \rangle)$  of the condensate, with the three components given by  $(\langle b_{i,s,\uparrow}^\dagger \sum_{\nu} b_{i,p_{\nu,\downarrow}} + \text{H.c.} \rangle, \langle -ib_{i,s,\uparrow}^\dagger \sum_{\nu} b_{i,p_{\nu,\downarrow}} + \text{H.c.} \rangle, \langle n_{i,s,\uparrow} - \sum_{\nu} n_{i,p_{\nu,\downarrow}} \rangle)$  with  $\nu = x, y$ . Here, the spin texture in  $x-y$  plane  $(\langle \sigma_{i,x} \rangle, \langle \sigma_{i,y} \rangle)$  given in Fig.4(c) shows a topological vortex lattice structure characterized by vortex (B) and anti-vortex (A) distributions, corresponding to the negative (B) and positive (A) OAM cluster centers, respectively. Further, the spin component along  $z$  direction  $\langle \sigma_{i,z} \rangle$  in Fig.4(d) exhibits another staggered clusters pattern, with a period of  $1/\sqrt{2}$  that of OAM patterns. From the three spin components the combined whole spin texture  $\langle \sigma_i \rangle$  forms a topological skyrmion lattice structure whose periodicity matches the OAM pattern. With the nontrivial topology encoded in the real space and in the momentum space (for quasiparticles), the superfluidity of  $|G\rangle$  renders an unprecedented topological SOSS phase breaking both lattice translation symmetry and  $U(1)$  symmetry, as predicted in the present orbital optical Raman lattice.

*Conclusion.* We explore the exotic many-body quantum phases by proposing an orbital optical Raman lattice scheme that innovatively combines the synthetic SOC and  $p$ -orbital condensates. We find that the competition between the Raman-induced SOC and  $p$ -orbital interaction can lead to two novel high-orbital condensed states: the UAMSF phase with uniform OAM order, which hosts global chiral edge excitations, and the 2D SOSS phase, characterized by a staggered OAM pattern and a topological skyrmion structure for spin texture, with opposite topological boundary excitations in neighboring OAM clusters. Unlike the double-well lattice for  $p$ -orbital systems [69, 71, 72, 75–78], the present orbital optical Raman lattice exhibits full controllability: both

the magnitude and the exact form of the Raman-induced  $s - p$  coupling can be independently and precisely controlled, leading to the nontrivial competitive interplay. Furthermore, we design a minimal experimental scheme based on cold atom platform, and the lifetime of the high-orbital many-body quantum phases is also discussed in [80]. Our work provides a new perspective on the further study of SOC and high-orbital physics in optical lattices, and will advance the experimental realization of super-solid phases without long-range interactions.

*Acknowledgments.* We thank Xin-Chi Zhou, Ting-Fung Jeffrey Poon, and Ye-Bing Zhang for valuable discussions. This work was supported by National Key Research and Development Program of China (No. 2021YFA1400900), the National Natural Science Foundation of China (Grants No. 12104205, No. 12261160368, and No. 11921005), and the Innovation Program for Quantum Science and Technology (Grant No. 2021ZD0302000) (Z.H.H., K.H.M., B.Z.W., X.J.L.), and by U.S. AFOSR Grant No. FA9550-23-1-0598 (W.V.L.).

---

\* These authors contributed equally to this work.

† xiongjunliu@pku.edu.cn

- [1] I. Bloch, J. Dalibard, and W. Zwerger, Many-body physics with ultracold gases, *Rev. Mod. Phys.* **80**, 885 (2008).
- [2] C. Gross and I. Bloch, Quantum simulations with ultracold atoms in optical lattices, *Science* **357**, 995 (2017).
- [3] D. Jaksch and P. Zoller, Creation of effective magnetic fields in optical lattices: the hofstadter butterfly for cold neutral atoms, *New Journal of Physics* **5**, 56 (2003).
- [4] G. Juzeliūnas and P. Öhberg, Slow light in degenerate fermi gases, *Phys. Rev. Lett.* **93**, 033602 (2004).
- [5] K. Osterloh, M. Baig, L. Santos, P. Zoller, and M. Lewenstein, Cold atoms in non-abelian gauge potentials: From the Hofstadter "moth" to lattice gauge theory, *Phys. Rev. Lett.* **95**, 010403 (2005).
- [6] J. Ruseckas, G. Juzeliūnas, P. Öhberg, and M. Fleischhauer, Non-abelian gauge potentials for ultracold atoms with degenerate dark states, *Phys. Rev. Lett.* **95**, 010404 (2005).
- [7] X.-J. Liu, H. Jing, X. Liu, and M.-L. Ge, Generation of two-flavor vortex atom laser from a five-state medium, *The European Physical Journal D-Atomic, Molecular, Optical and Plasma Physics* **37**, 261 (2006).
- [8] J. Dalibard, F. Gerbier, G. Juzeliūnas, and P. Öhberg, Colloquium: Artificial gauge potentials for neutral atoms, *Rev. Mod. Phys.* **83**, 1523 (2011).
- [9] N. Goldman, G. Juzeliūnas, P. Öhberg, and I. B. Spielman, Light-induced gauge fields for ultracold atoms, *Reports on Progress in Physics* **77**, 126401 (2014).
- [10] H.-R. Chen, K.-Y. Lin, P.-K. Chen, N.-C. Chiu, J.-B. Wang, C.-A. Chen, P. Huang, S.-K. Yip, Y. Kawaguchi, and Y.-J. Lin, Spin-orbital-angular-momentum coupled bose-einstein condensates, *Phys. Rev. Lett.* **121**, 113204 (2018).
- [11] M. Aidelsburger, L. Barbiero, A. Bermudez, T. Chanda, A. Dauphin, D. González-Cuadra, P. R. Grzybowski, S. Hands, F. Jendrzejewski, J. Jünemann, *et al.*, Cold atoms meet lattice gauge theory, *Philosophical Transactions of the Royal Society A* **380**, 20210064 (2022).
- [12] X.-J. Liu, M. F. Borunda, X. Liu, and J. Sinova, Effect of induced spin-orbit coupling for atoms via laser fields, *Phys. Rev. Lett.* **102**, 046402 (2009).
- [13] G. Juzeliūnas, J. Ruseckas, and J. Dalibard, Generalized rashba-dresselhaus spin-orbit coupling for cold atoms, *Phys. Rev. A* **81**, 053403 (2010).
- [14] Y.-J. Lin, K. Jiménez-García, and I. B. Spielman, Spin-orbit-coupled bose-einstein condensates, *Nature* **471**, 83 (2011).
- [15] D. L. Campbell, G. Juzeliūnas, and I. B. Spielman, Realistic rashba and dresselhaus spin-orbit coupling for neutral atoms, *Phys. Rev. A* **84**, 025602 (2011).
- [16] J. D. Sau, R. Sensarma, S. Powell, I. Spielman, and S. D. Sarma, Chiral rashba spin textures in ultracold fermi gases, *Phys. Rev. B* **83**, 140510 (2011).
- [17] P. Wang, Z.-Q. Yu, Z. Fu, J. Miao, L. Huang, S. Chai, H. Zhai, and J. Zhang, Spin-orbit coupled degenerate fermi gases, *Phys. Rev. Lett.* **109**, 095301 (2012).
- [18] L. W. Cheuk, A. T. Sommer, Z. Hadzibabic, T. Yefsah, W. S. Bakr, and M. W. Zwierlein, Spin-injection spectroscopy of a spin-orbit coupled fermi gas, *Phys. Rev. Lett.* **109**, 095302 (2012).
- [19] B. M. Anderson, G. Juzeliūnas, V. M. Galitski, and I. B. Spielman, Synthetic 3d spin-orbit coupling, *Phys. Rev. Lett.* **108**, 235301 (2012).
- [20] V. Galitski and I. B. Spielman, Spin-orbit coupling in quantum gases, *Nature* **494**, 49 (2013).
- [21] X.-J. Liu, K. T. Law, and T. K. Ng, Realization of 2d spin-orbit interaction and exotic topological orders in cold atoms, *Phys. Rev. Lett.* **112**, 086401 (2014).
- [22] H. Zhai, Degenerate quantum gases with spin-orbit coupling: a review, *Reports on Progress in Physics* **78**, 026001 (2015).
- [23] Z. Wu, L. Zhang, W. Sun, X.-T. Xu, B.-Z. Wang, S.-C. Ji, Y. Deng, S. Chen, X.-J. Liu, and J.-W. Pan, Realization of two-dimensional spin-orbit coupling for bose-einstein condensates, *Science* **354**, 83 (2016).
- [24] N. Q. Burdick, Y. Tang, and B. L. Lev, Long-lived spin-orbit-coupled degenerate dipolar fermi gas, *Phys. Rev. X* **6**, 031022 (2016).
- [25] B. Song, C. He, S. Zhang, E. Hajiyev, W. Huang, X.-J. Liu, and G.-B. Jo, Spin-orbit-coupled two-electron fermi gases of ytterbium atoms, *Phys. Rev. A* **94**, 061604 (2016).
- [26] S. Kolkowitz, S. Bromley, T. Bothwell, M. Wall, G. Marti, A. Koller, X. Zhang, A. Rey, and J. Ye, Spin-orbit-coupled fermions in an optical lattice clock, *Nature* **542**, 66 (2017).
- [27] L. Zhang and X.-J. Liu, Spin-orbit coupling and topological phases for ultracold atoms, in *Synthetic Spin-Orbit Coupling in Cold Atoms* (World Scientific, 2018) pp. 1–87.
- [28] B.-Z. Wang, Y.-H. Lu, W. Sun, S. Chen, Y. Deng, and X.-J. Liu, Dirac-, rashba-, and weyl-type spin-orbit couplings: Toward experimental realization in ultracold atoms, *Phys. Rev. A* **97**, 011605 (2018).
- [29] L. Huang, Z. Meng, P. Wang, P. Peng, S.-L. Zhang, L. Chen, D. Li, Q. Zhou, and J. Zhang, Experimental realization of two-dimensional synthetic spin-orbit cou-

- pling in ultracold fermi gases, *Nat. Phys.* **12**, 540 (2016).
- [30] Z. Meng, L. Huang, P. Peng, D. Li, L. Chen, Y. Xu, C. Zhang, P. Wang, and J. Zhang, Experimental observation of a topological band gap opening in ultracold fermi gases with two-dimensional spin-orbit coupling, *Phys. Rev. Lett.* **117**, 235304 (2016).
- [31] W. Sun, B.-Z. Wang, X.-T. Xu, C.-R. Yi, L. Zhang, Z. Wu, Y. Deng, X.-J. Liu, S. Chen, and J.-W. Pan, Highly controllable and robust 2d spin-orbit coupling for quantum gases, *Phys. Rev. Lett.* **121**, 150401 (2018).
- [32] W. Sun, C.-R. Yi, B.-Z. Wang, W.-W. Zhang, B. C. Sanders, X.-T. Xu, Z.-Y. Wang, J. Schmiedmayer, Y. Deng, X.-J. Liu, S. Chen, and J.-W. Pan, Uncover topology by quantum quench dynamics, *Phys. Rev. Lett.* **121**, 250403 (2018).
- [33] Z.-Y. Wang, X.-C. Cheng, B.-Z. Wang, J.-Y. Zhang, Y.-H. Lu, C.-R. Yi, S. Niu, Y. Deng, X.-J. Liu, S. Chen, *et al.*, Realization of an ideal weyl semimetal band in a quantum gas with 3d spin-orbit coupling, *Science* **372**, 271 (2021).
- [34] M.-C. Liang, Y.-D. Wei, L. Zhang, X.-J. Wang, H. Zhang, W.-W. Wang, W. Qi, X.-J. Liu, and X. Zhang, Realization of qi-wu-zhang model in spin-orbit-coupled ultracold fermions, *Phys. Research* **5**, L012006 (2023).
- [35] E. Zhao, Z. Wang, C. He, T. F. J. Poon, K. K. Pak, Y.-J. Liu, P. Ren, X.-J. Liu, and G.-B. Jo, Two-dimensional non-hermitian skin effect in an ultracold fermi gas, *arXiv preprint arXiv:2311.07931* (2023).
- [36] X.-C. Zhou, T.-H. Yang, Z.-Y. Wang, and X.-J. Liu, Non-abelian dynamical gauge field and topological superfluids in optical raman lattice, *arXiv preprint arXiv:2309.12923* (2023).
- [37] N. Goldman, I. Satija, P. Nikolic, A. Bermudez, M. A. Martin-Delgado, M. Lewenstein, and I. Spielman, Realistic time-reversal invariant topological insulators with neutral atoms, *Phys. Rev. Lett.* **105**, 255302 (2010).
- [38] B. Béri and N. Cooper, Z2 topological insulators in ultracold atomic gases, *Phys. Rev. Lett.* **107**, 145301 (2011).
- [39] X.-J. Liu, Z.-X. Liu, and M. Cheng, Manipulating topological edge spins in a one-dimensional optical lattice, *Phys. Rev. Lett.* **110**, 076401 (2013).
- [40] G. Jotzu, M. Messer, R. Desbuquois, M. Lebrat, T. Uehlinger, D. Greif, and T. Esslinger, Experimental realization of the topological haldane model with ultracold fermions, *Nature* **515**, 237 (2014).
- [41] S.-T. Wang, D.-L. Deng, and L.-M. Duan, Probe of three-dimensional chiral topological insulators in an optical lattice, *Phys. Rev. Lett.* **113**, 033002 (2014).
- [42] B. Song, L. Zhang, C. He, T. F. J. Poon, E. H. H. Jijev, S. Zhang, X.-J. Liu, and G.-B. Jo, Observation of symmetry-protected topological band with ultracold fermions, *Sci. Adv* **4** (2018).
- [43] C.-R. Yi, L. Zhang, L. Zhang, R.-H. Jiao, X.-C. Cheng, Z.-Y. Wang, X.-T. Xu, W. Sun, X.-J. Liu, S. Chen, *et al.*, Observing topological charges and dynamical bulk-surface correspondence with ultracold atoms, *Phys. Rev. Lett.* **123**, 190603 (2019).
- [44] M. Boninsegni and N. V. Prokof'ev, Colloquium: Supersolids: What and where are they?, *Rev. Mod. Phys.* **84**, 759 (2012).
- [45] H. Ritsch, P. Domokos, F. Brennecke, and T. Esslinger, Cold atoms in cavity-generated dynamical optical potentials, *Rev. Mod. Phys.* **85**, 553 (2013).
- [46] A. Recati and S. Stringari, Supersolidity in ultracold dipolar gases, *Nature Reviews Physics* **5**, 735 (2023).
- [47] J.-R. Li, J. Lee, W. Huang, S. Burchesky, B. Shteynas, F. Ç. Top, A. O. Jamison, and W. Ketterle, A stripe phase with supersolid properties in spin-orbit-coupled bose-einstein condensates, *Nature* **543**, 91 (2017).
- [48] F. Böttcher, J.-N. Schmidt, M. Wenzel, J. Hertkorn, M. Guo, T. Langen, and T. Pfau, Transient supersolid properties in an array of dipolar quantum droplets, *Phys. Rev. X* **9**, 011051 (2019).
- [49] L. Tanzi, E. Lucioni, F. Famà, J. Catani, A. Fioretti, C. Gabbanini, R. N. Bisset, L. Santos, and G. Modugno, Observation of a dipolar quantum gas with metastable supersolid properties, *Phys. Rev. Lett.* **122**, 130405 (2019).
- [50] L. Chomaz, D. Petter, P. Ilzhöfer, G. Natale, A. Trautmann, C. Politi, G. Durastante, R. Van Bijnen, A. Patscheider, M. Sohmen, *et al.*, Long-lived and transient supersolid behaviors in dipolar quantum gases, *Phys. Rev. X* **9**, 021012 (2019).
- [51] M. A. Norcia, C. Politi, L. Klaus, E. Poli, M. Sohmen, M. J. Mark, R. N. Bisset, L. Santos, and F. Ferlaino, Two-dimensional supersolidity in a dipolar quantum gas, *Nature* **596**, 357 (2021).
- [52] T. Bland, E. Poli, C. Politi, L. Klaus, M. A. Norcia, F. Ferlaino, L. Santos, and R. N. Bisset, Two-dimensional supersolid formation in dipolar condensates, *Phys. Rev. Lett.* **128**, 195302 (2022).
- [53] E. Casotti, E. Poli, L. Klaus, A. Litvinov, C. Ulm, C. Politi, M. J. Mark, T. Bland, and F. Ferlaino, Observation of vortices in a dipolar supersolid, *Nature* **635**, 327 (2024).
- [54] J. Léonard, A. Morales, P. Zupancic, T. Esslinger, and T. Donner, Supersolid formation in a quantum gas breaking a continuous translational symmetry, *Nature* **543**, 87 (2017).
- [55] J. Léonard, A. Morales, P. Zupancic, T. Donner, and T. Esslinger, Monitoring and manipulating higgs and goldstone modes in a supersolid quantum gas, *Science* **358**, 1415 (2017).
- [56] E. Zhao and W. V. Liu, Orbital order in mott insulators of spinless p-band fermions, *Phys. Rev. Lett.* **100**, 160403 (2008).
- [57] X.-J. Liu, X. Liu, C. Wu, and J. Sinova, Quantum anomalous hall effect with cold atoms trapped in a square lattice, *Phys. Rev. A* **81**, 033622 (2010).
- [58] Z. Cai, Y. Wang, and C. Wu, Stable fulde-ferrell-larkin-ovchinnikov pairing states in two-dimensional and three-dimensional optical lattices, *Phys. Rev. A* **83**, 063621 (2011).
- [59] M. Lewenstein and W. V. Liu, Orbital dance, *Nat. Phys.* **7**, 101 (2011).
- [60] X. Li, E. Zhao, and W. Vincent Liu, Topological states in a ladder-like optical lattice containing ultracold atoms in higher orbital bands, *Nat Commun* **4**, 1523 (2013).
- [61] T. Sowiński, M. Łącki, O. Dutta, J. Pietraszewicz, P. Sierant, M. Gajda, J. Zakrzewski, and M. Lewenstein, Tunneling-induced restoration of the degeneracy and the time-reversal symmetry breaking in optical lattices, *Phys. Rev. Lett.* **111**, 215302 (2013).
- [62] O. Dutta, M. Gajda, P. Hauke, M. Lewenstein, D.-S. Lühmann, B. A. Malomed, T. Sowiński, and J. Zakrzewski, Non-standard hubbard models in optical lattices: a review, *Reports on Progress in Physics* **78**,

- 066001 (2015).
- [63] X. Li and W. V. Liu, Physics of higher orbital bands in optical lattices: a review, *Reports on Progress in Physics* **79**, 116401 (2016).
- [64] A. Isacsson and S. M. Girvin, Multiflavor bosonic hubbard models in the first excited bloch band of an optical lattice, *Phys. Rev. A* **72**, 053604 (2005).
- [65] A. B. Kuklov, Unconventional strongly interacting bose-einstein condensates in optical lattices, *Phys. Rev. Lett.* **97**, 110405 (2006).
- [66] W. V. Liu and C. Wu, Atomic matter of nonzero-momentum bose-einstein condensation and orbital current order, *Phys. Rev. A* **74**, 013607 (2006).
- [67] C. Wu, W. V. Liu, J. Moore, and S. D. Sarma, Quantum stripe ordering in optical lattices, *Phys. Rev. Lett.* **97**, 190406 (2006).
- [68] J. Larson, A. Collin, and J.-P. Martikainen, Multiband bosons in optical lattices, *Phys. Rev. A* **79**, 033603 (2009).
- [69] G. Wirth, M. Ölschläger, and A. Hemmerich, Evidence for orbital superfluidity in the p-band of a bipartite optical square lattice, *Nat. Phys.* **7**, 147 (2011).
- [70] X. Li, Z. Zhang, and W. V. Liu, Time-reversal symmetry breaking of p-orbital bosons in a one-dimensional optical lattice, *Phys. Rev. Lett.* **108**, 175302 (2012).
- [71] Z.-F. Xu, L. You, A. Hemmerich, and W. V. Liu,  $\pi$ -flux dirac bosons and topological edge excitations in a bosonic chiral p-wave superfluid, *Phys. Rev. Lett.* **117**, 085301 (2016).
- [72] M. Di Liberto, A. Hemmerich, and C. Morais Smith, Topological varma superfluid in optical lattices, *Phys. Rev. Lett.* **117**, 163001 (2016).
- [73] Y.-Q. Wang and X.-J. Liu, Dirac and topological phonons with spin-orbital entangled orders (2017), arXiv:1710.02070 [cond-mat.quant-gas].
- [74] Y. Li, J. Yuan, A. Hemmerich, and X. Li, Rotation-symmetry-enforced coupling of spin and angular momentum for p-orbital bosons, *Phys. Rev. Lett.* **121**, 093401 (2018).
- [75] J.-S. Pan, W. V. Liu, and X.-J. Liu, Emergence of the unconventional type-ii nambu-goldstone modes with topological origin in bose superfluids, *Phys. Rev. Lett.* **125**, 260402 (2020).
- [76] S. Jin, W. Zhang, X. Guo, X. Chen, X. Zhou, and X. Li, Evidence of potts-nematic superfluidity in a hexagonal sp 2 optical lattice, *Phys. Rev. Lett.* **126**, 035301 (2021).
- [77] X.-Q. Wang, G.-Q. Luo, J.-Y. Liu, W. V. Liu, A. Hemmerich, and Z.-F. Xu, Evidence for an atomic chiral superfluid with topological excitations, *Nature* **596**, 227 (2021).
- [78] G.-H. Huang, Z.-F. Xu, and Z. Wu, Intrinsic anomalous hall effect in a bosonic chiral superfluid, *Phys. Rev. Lett.* **129**, 185301 (2022).
- [79] X.-Q. Wang, G.-Q. Luo, J.-Y. Liu, G.-H. Huang, Z.-X. Li, C. Wu, A. Hemmerich, and Z.-F. Xu, Evidence for quantum stripe ordering in a triangular optical lattice, *Phys. Rev. Lett.* **131**, 226001 (2023).
- [80] See supplementary material for the details on the experimental realization scheme of the orbital optical Raman lattice, the derivation of lattice model Hamiltonian, the Bogoliubov theory of quasiparticle excitations, and the discussion of lifetime.
- [81] K. Sun, W. V. Liu, A. Hemmerich, and S. Das Sarma, Topological semimetal in a fermionic optical lattice, *Nat. Phys.* **8**, 67 (2012).
- [82] P. J. Van Laarhoven, E. H. Aarts, P. J. van Laarhoven, and E. H. Aarts, *Simulated annealing* (Springer, 1987).
- [83] R. Shindou, R. Matsumoto, S. Murakami, and J.-i. Ohe, Topological chiral magnonic edge mode in a magnonic crystal, *Phys. Rev. B* **87**, 174427 (2013).

# Supplementary Material

Zhi-Hao Huang<sup>\*1,2</sup>, Kou-Han Ma<sup>\*1,2</sup>, Bao-Zong Wang<sup>1,2</sup>, W. Vincent Liu<sup>3,4</sup>, and Xiong-Jun Liu<sup>†1,2,4</sup>

<sup>1</sup>International Center for Quantum Materials and School of Physics, Peking University, Beijing 100871, China

<sup>2</sup>Hefei National Laboratory, Hefei 230088, China

<sup>3</sup>Department of Physics and Astronomy and IQ Initiative, University of Pittsburgh, Pittsburgh, PA 15260, USA

<sup>4</sup>International Quantum Academy, Shenzhen 518048, China

December 13, 2024

In this supplementary material, we first demonstrate the experimental realization of the continuous Hamiltonian described in the main text using the orbital optical Raman lattice, and then derive the corresponding lattice model Hamiltonian with appropriate parameters. Next, we use the Bogoliubov theory to obtain the quasiparticle excitation spectrum for the uniform angular momentum superfluid phase and the two-dimensional spin-orbital supersolid phase. The lifetimes of the exotic many-body quantum phases are also discussed qualitatively.

## Contents

<b>A</b>	<b>Orbital optical Raman lattice scheme</b>	<b>1</b>
A.1	Optical lattice . . . . .	2
A.2	Raman field . . . . .	2
<b>B</b>	<b>Model Hamiltonian</b>	<b>3</b>
B.1	Non-interacting part . . . . .	3
B.2	Interacting part . . . . .	4
B.3	Model parameters . . . . .	5
<b>C</b>	<b>Bogoliubov mean field theory</b>	<b>6</b>
C.1	Uniform angular momentum superfluid phase . . . . .	6
C.2	Two-dimensional spin-orbital supersolid phase . . . . .	7
<b>D</b>	<b>Lifetime of the exotic many-body ground states</b>	<b>8</b>

## A Orbital optical Raman lattice scheme

The optical Raman lattice plays a significant role in investigating the use of cold atoms to simulate exotic topological quantum matters. In this section, we will introduce the orbital optical Raman lattice scheme for realizing the continuous Hamiltonian shown in the main text.

---

\*These authors contribute equally to this work

†xiongjunliu@pku.edu.cn



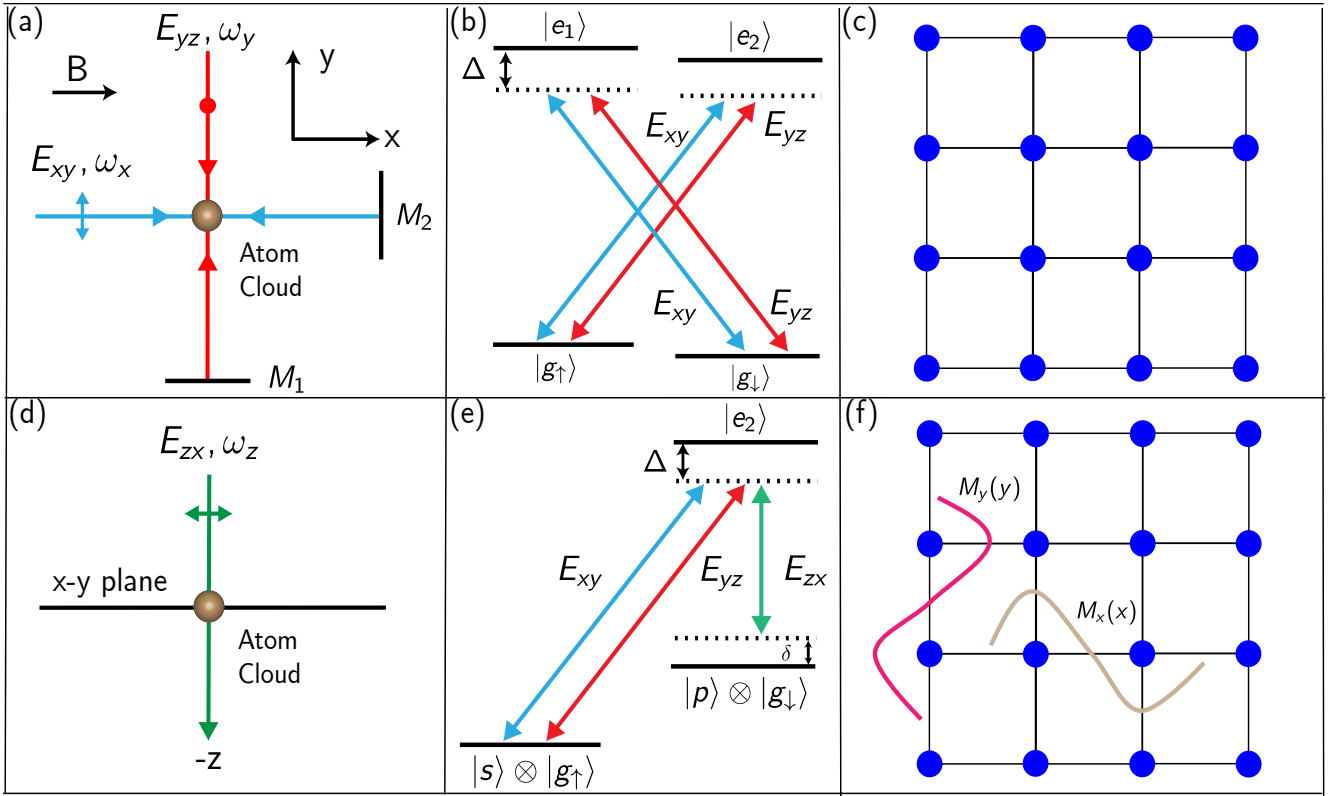


Figure 1: (a) Applying two laser beams  $\mathbf{E}_{xy} = \hat{y}E_0 \cos(k_0x)$  and  $\mathbf{E}_{yz} = \hat{z}E_0 \cos(k_0y)$  can realize a square lattice. Here the bias magnetic field is set along the  $x$  direction. (b) Both  $\mathbf{E}_{xy}$  and  $\mathbf{E}_{yz}$  can induce the transition from the ground states with  $m_F$  to excited states with  $m_F + 1$  and  $m_F - 1$ , where the hyperfine states  $|1, -1\rangle$  and  $|1, 0\rangle$  of  $^{87}\text{Rb}$  are used to mimic the ground states  $|g_{\uparrow, \downarrow}\rangle$ . (c) Square optical lattice  $V(\mathbf{r})$ . (d) Applying another plane wave laser  $\mathbf{E}_{zx}$  with polarization along  $x$  direction based on the setup in (a). (e) There is a single  $\mathbf{A}$  configuration where the Raman potentials  $M_x(x)$  and  $M_y(y)$  can be generated by the laser pairs  $(\mathbf{E}_{xy}, \mathbf{E}_{zx})$  and  $(\mathbf{E}_{yz}, \mathbf{E}_{zx})$ , respectively. (f) Raman field  $M(\mathbf{r})$ . Notice that the Raman field has twice the periodicity of the lattice potential.

## A.1 Optical lattice

We first generate the square lattice on  $x - y$  plane using the standing waves  $\mathbf{E}_{xy} = \hat{y}E_0 \cos(k_0x)$  and  $\mathbf{E}_{yz} = \hat{z}E_0 \cos(k_0y)$  [Fig.1 (a)], where  $k_0 = \frac{\pi}{a}$ . Here, the standing waves  $\mathbf{E}_{xy}$  and  $\mathbf{E}_{yz}$  are linearly polarized along  $y$  and  $z$  directions, respectively, eliminating the interference term between them. Note that the bias magnetic field is set along the  $x$  direction. As shown in Fig.1 (b), both  $\mathbf{E}_{xy}$  (blue line) and  $\mathbf{E}_{yz}$  (red line) can induce the transition from the ground state with  $m_F$  to the excited states with  $m_F + 1$  and  $m_F - 1$ . Here, we select two hyperfine states  $|1, -1\rangle$  and  $|1, 0\rangle$  of  $^{87}\text{Rb}$  to mimic the ground states  $|g_{\uparrow, \downarrow}\rangle$  with  $|1, -1\rangle = |g_{\uparrow}\rangle$ ,  $|1, 0\rangle = |g_{\downarrow}\rangle$ . When the detuning is much larger than the Rabi frequency of the standing waves ( $|\Delta| \gg |\Omega(\mathbf{E}_{xy}, \mathbf{E}_{yz})|$ ), the atom-light couplings contribute to diagonal potentials for the ground states  $|g_{\uparrow, \downarrow}\rangle$ , given by  $V_{\uparrow} = \hbar(|\Omega_{\mathbf{E}_{xy}}|^2/\Delta + |\Omega_{\mathbf{E}_{yz}}|^2/\Delta)$  and  $V_{\downarrow} = \hbar(|\Omega_{\mathbf{E}_{xy}}|^2/\Delta + |\Omega_{\mathbf{E}_{yz}}|^2/\Delta)$ , where  $\Delta$  denotes the red detuning for  $\mathbf{E}_{xy}$  and  $\mathbf{E}_{yz}$ . Thus, the optical lattice potential reads

$$V(\mathbf{r}) = -V_0[\cos^2(k_0x) + \cos^2(k_0y)], \quad (1)$$

where  $V_0 = \frac{\hbar E_0^2}{|\Delta|}$  ( $\Delta < 0$ ). The configuration of optical lattice in Eq.(1) is shown in Fig.1 (c).

## A.2 Raman field

As shown in Fig.1 (d), the Raman potentials can be generated by adding another plane wave laser  $\mathbf{E}_{zx} = \hat{x}E_z e^{-ik_z z}$ , which propagates along the  $z$  axis and is polarized along the  $x$  axis. The applied plane wave laser  $\mathbf{E}_{zx}$  can induce the  $\pi$  transitions from ground states  $|g_{\uparrow}\rangle$  and  $|g_{\downarrow}\rangle$  to the excited states  $|e_1\rangle$  and  $|e_2\rangle$ , respectively. As shown in Fig.1 (e), we tune the frequency of the plane wave  $\mathbf{E}_{zx}$  so that the atom-light couplings can occur between  $|s\rangle \otimes |g_{\uparrow}\rangle$ ,  $|p\rangle \otimes |g_{\downarrow}\rangle$ , and the excited state  $|e_2\rangle$ , forming a single  $\mathbf{A}$ -type configuration [Fig.1 (e)]. Here,  $|s\rangle$  and  $|p\rangle$  denote the

local orbital states. Through this configuration, the Raman potentials  $M_x(x)$  and  $M_y(y)$  can be generated by the laser pairs  $(\mathbf{E}_{xy}, \mathbf{E}_{zx})$  and  $(\mathbf{E}_{yz}, \mathbf{E}_{zx})$ , respectively. When  $|\Delta| \gg |\Omega_{\mathbf{E}_{xy}}|, |\Omega_{\mathbf{E}_{zx}}| (|\Omega_{\mathbf{E}_{yz}}|, |\Omega_{\mathbf{E}_{zx}}|)$  and the two-photon off resonance  $\delta$  is smaller than the coupling strength  $|\Omega_{\mathbf{E}_{xy}}\Omega_{\mathbf{E}_{zx}}/\Delta|$  ( $|\Omega_{\mathbf{E}_{yz}}\Omega_{\mathbf{E}_{zx}}/\Delta|$ ), the two-photon processes in the  $\mathbf{A}$ -type configuration are dominant and induce the Raman couplings between  $|s\rangle \otimes |g_\uparrow\rangle$  and  $|p\rangle \otimes |g_\downarrow\rangle$ , where  $\Omega$  denotes the Rabi frequency of the lasers. Then the Raman field is given by [Fig.1 (f)]

$$M(\mathbf{r}) = -M_0[\cos(k_0x) + \cos(k_0y)](|s\rangle \otimes |g_\uparrow\rangle\langle g_\downarrow| \otimes \langle p| + \text{H.c.}), \quad (2)$$

where  $M_0 = \frac{\hbar E_0 E_z}{|\Delta|}$ . The two-photon detuning also contributes to the Zeeman splitting  $m_z = \hbar\delta/2$ .

## B Model Hamiltonian

In this section, we derive the model Hamiltonian  $\hat{H} = \hat{H}_0 + \hat{H}_{\text{int}}$  for the interacting ultracold Bose gases trapped in a square orbital optical Raman lattice. Here,  $\hat{H}_0$  and  $\hat{H}_{\text{int}}$  represent the non-interacting and interacting parts, respectively. We also provide the appropriate model parameters to facilitate the experimental realization.

### B.1 Non-interacting part

We first start from the non-interacting continuous Hamiltonian

$$H_0 = \frac{p_{\mathbf{r}}^2}{2M} + V(\mathbf{r}) + M(\mathbf{r})\sigma_x + m_z\sigma_z, \quad (3)$$

where Pauli matrices  $\boldsymbol{\sigma}$  act on the two-dimensional space spanned by  $|s\rangle \otimes |g_\uparrow\rangle$  and  $|p\rangle \otimes |g_\downarrow\rangle$ . Moreover,  $V(\mathbf{r})$  and  $M(\mathbf{r})$  represent respectively the optical lattice potential and Raman field with

$$V(\mathbf{r}) = -V_0[\cos^2(\frac{\pi}{a}x) + \cos^2(\frac{\pi}{a}y)], \quad M(\mathbf{r}) = -M_0[\cos(\frac{\pi}{a}x) + \cos(\frac{\pi}{a}y)]. \quad (4)$$

Here  $V_0$ ,  $M_0$ , and  $a$  denote the lattice depth, Raman strength, and lattice constant, respectively. For convenience, we take  $a = 1$ .  $m_z$  is the effective Zeeman field. According to the second quantization, Eq. (3) can be rewritten as

$$\hat{H}_0 = \int d\mathbf{r} \Psi^\dagger(\mathbf{r}) \left[ \frac{p_{\mathbf{r}}^2}{2M} + V(\mathbf{r}) + M(\mathbf{r})\sigma_x + m_z\sigma_z \right] \Psi(\mathbf{r}). \quad (5)$$

Here  $\Psi^\dagger(\mathbf{r}) = \sum_{il\sigma} b_{i,l,\sigma}^\dagger \phi_{l\sigma}^*(\mathbf{r} - \mathbf{r}_i)$  ( $l = s, p_x, p_y; \sigma = \uparrow, \downarrow$ ) is the field operator and  $b_{i,l,\sigma}^\dagger$  represents creating a Boson with orbital  $l$  and spin  $\sigma$  at lattice site  $\mathbf{r}_i$ . Moreover,  $\phi_{l,\sigma}(\mathbf{r} - \mathbf{r}_i) = \psi_l(\mathbf{r} - \mathbf{r}_i) \otimes \chi_\sigma$  denotes is the Wannier function at  $\mathbf{r}_i$ , where  $\psi_l(\mathbf{r} - \mathbf{r}_i)$  and  $\chi_\sigma$  denote the corresponding spatial and spin components, respectively.

As discussed in the previous section, Raman coupling occurs between the  $|s\rangle \otimes |g_\uparrow\rangle$  and  $|p\rangle \otimes |g_\downarrow\rangle$ , which can effectively bring the  $s_\uparrow$  and  $p_{x\downarrow}$  ( $p_{y\downarrow}$ ) orbitals closer together under the rotating coordinate system, separating them from other orbitals. As a consequence, within the subspace spanned by  $(s_\uparrow, p_{x\downarrow}, p_{y\downarrow})$ , the field operator can be approximated as  $\Psi^\dagger(\mathbf{r}) \approx \sum_i \left[ b_{i,s,\uparrow}^\dagger \phi_{s\uparrow}^*(\mathbf{r} - \mathbf{r}_i) + b_{i,p_x,\downarrow}^\dagger \phi_{p_x\downarrow}^*(\mathbf{r} - \mathbf{r}_i) + b_{i,p_y,\downarrow}^\dagger \phi_{p_y\downarrow}^*(\mathbf{r} - \mathbf{r}_i) \right]$ . Now we can obtain the tight-binding Hamiltonian  $\hat{H}_0 = \hat{H}_{\text{sc}} + \hat{H}_{\text{sf}}$  straightforwardly, where  $\hat{H}_{\text{sc}}$  and  $\hat{H}_{\text{sf}}$  represent the spin-conserved and spin-flipped parts induced by the optical lattice potential  $V(\mathbf{r})$  and the Raman field  $M(\mathbf{r})$ , respectively. Specifically,

$$\begin{aligned} \hat{H}_{\text{sc}} = & -t_s \sum_{\langle i,j \rangle} b_{i,s,\uparrow}^\dagger b_{j,s,\uparrow} + \sum_{i\mu\nu} t_p^{\mu\nu} \left( b_{i,p_\mu,\downarrow}^\dagger b_{i+e_\nu,p_\mu,\downarrow} + \text{H.c.} \right) \\ & + (\mu_s + m_z) \sum_i n_{i,s,\uparrow} + (\mu_p - m_z) \sum_{i\nu} n_{i,p_\nu,\downarrow}, \end{aligned} \quad (6)$$

$$\hat{H}_{\text{sf}} = \sum_{i,\nu,\delta_\nu} -t_{s\sigma}^{(i,i+\delta_\nu)} b_{i,p_\nu,\downarrow}^\dagger b_{i+\delta_\nu,s,\uparrow} + \text{H.c.}, \quad (7)$$

where  $n_{i,s,\uparrow} = b_{i,s,\uparrow}^\dagger b_{i,s,\uparrow}$ ,  $n_{i,p_\nu,\downarrow} = b_{i,p_\nu,\downarrow}^\dagger b_{i,p_\nu,\downarrow}$ , and  $t_p^{\mu\nu} = t_p^\parallel \cdot \delta_{\mu\nu} - t_p^\perp \cdot (1 - \delta_{\mu\nu})$  ( $\mu, \nu = x, y$ ). “sgn” is a sign function and  $\delta_\nu = \pm e_\nu$ .  $\mu_s$  and  $\mu_p$  represent the effective  $s$  and  $p$  orbitals on-site energies, respectively. Furthermore,

the corresponding spin-conserved hopping coefficients are given by

$$\begin{aligned}
t_s &= - \int d\mathbf{r} \phi_{s,\uparrow}^*(\mathbf{r} - \mathbf{r}_i) \left[ \frac{p_r^2}{2M} + V(\mathbf{r}) \right] \phi_{s,\uparrow}(\mathbf{r} - \mathbf{r}_{i+\mathbf{e}_x(y)}), \\
t_p^\parallel &= \int d\mathbf{r} \phi_{p_x(y),\downarrow}^*(\mathbf{r} - \mathbf{r}_i) \left[ \frac{p_r^2}{2M} + V(\mathbf{r}) \right] \phi_{p_x(y),\downarrow}(\mathbf{r} - \mathbf{r}_{i+\mathbf{e}_x(y)}), \\
t_p^\perp &= - \int d\mathbf{r} \phi_{p_x(y),\downarrow}^*(\mathbf{r} - \mathbf{r}_i) \left[ \frac{p_r^2}{2M} + V(\mathbf{r}) \right] \phi_{p_x(y),\downarrow}(\mathbf{r} - \mathbf{r}_{i+\mathbf{e}_y(x)}),
\end{aligned} \tag{8}$$

As given in Eq.(4), the Raman field  $M(\mathbf{r})$  has twice the period of the optical lattice potential  $V(\mathbf{r})$ . Therefore, the spin-flipped hopping coefficient in Eq.(7) is staggered in  $\nu$  ( $\nu = x, y$ ) direction:  $t_{so}^{(i,i\pm\mathbf{e}_\nu)} = \pm(-1)^{i_\nu} t_{SO}$ , where

$$t_{SO} = M_0 \int d\mathbf{r} \psi_s^*(\mathbf{r} - \mathbf{r}_0) \cos(\pi\nu) \psi_{p_\nu}(\mathbf{r} - \mathbf{r}_{\mathbf{e}_\nu}). \tag{9}$$

Note that this staggered spin-flipped hopping has two important consequences. The staggered property implies that the coupling between  $s_\uparrow$  and  $p_x(y)_\downarrow$  states transfers  $\pi/a$  momentum, which effectively shifts the Brillouin zone by half along  $k_x$  ( $k_y$ ) direction for the  $p_x(y)_\downarrow$  states (relative to the  $s_\uparrow$  states). Here we can redefine the spin-down operator by a unitary transformation  $b_{i,p_\nu,\downarrow} \rightarrow -(-1)^{i_\nu} b_{i,p_\nu,\downarrow}$  to absorb this effect. Thus the tight-binding Hamiltonian  $\hat{H}_0$  can be rewritten as

$$\begin{aligned}
\hat{H}_0 &= -t_s \sum_{\langle i,j \rangle} b_{i,s,\uparrow}^\dagger b_{j,s,\uparrow} - \sum_i \sum_{\nu, \bar{\nu} \neq \nu} \left( t_p^\parallel b_{i,p_\nu,\downarrow}^\dagger b_{i+\mathbf{e}_\nu,p_\nu,\downarrow} + t_p^\perp b_{i,p_\nu,\downarrow}^\dagger b_{i+\mathbf{e}_{\bar{\nu}},p_\nu,\downarrow} + \text{H.c.} \right) \\
&+ t_{SO} \sum_{i,\nu,\delta_\nu} \left[ \text{sgn}(\delta_\nu) b_{i,p_\nu,\downarrow}^\dagger b_{i+\delta_\nu,s,\uparrow} + \text{H.c.} \right] + (\mu_s + m_z) \sum_i n_{i,s,\uparrow} + (\mu_p - m_z) \sum_{i\nu} n_{i,p_\nu,\downarrow}.
\end{aligned} \tag{10}$$

Performing a Fourier transformation, we can obtain the tight-binding Hamiltonian in momentum space

$$\hat{H}_0 = \sum_{\mathbf{k}} \mathcal{B}_{\mathbf{k}}^\dagger \mathcal{H}_0 \mathcal{B}_{\mathbf{k}} = \sum_{\mathbf{k}} \mathcal{B}_{\mathbf{k}}^\dagger \begin{pmatrix} \epsilon_{s_\uparrow}(\mathbf{k}) & -i2t_{SO} \sin k_x & -i2t_{SO} \sin k_y \\ i2t_{SO} \sin k_x & \epsilon_{p_{x\downarrow}}(\mathbf{k}) & \\ i2t_{SO} \sin k_y & & \epsilon_{p_{y\downarrow}}(\mathbf{k}) \end{pmatrix} \mathcal{B}_{\mathbf{k}}, \tag{11}$$

where  $\mathcal{B}_{\mathbf{k}}^\dagger = \left( b_{\mathbf{k},s_\uparrow}^\dagger \quad b_{\mathbf{k},p_{x\downarrow}}^\dagger \quad b_{\mathbf{k},p_{y\downarrow}}^\dagger \right)$ . The three diagonal elements  $\epsilon_{s_\uparrow}(\mathbf{k}) = \mu_s + m_z - 2t_s(\cos k_x + \cos k_y)$ ,  $\epsilon_{p_{x\downarrow}}(\mathbf{k}) = \mu_p - m_z - 2t_p^\parallel \cos k_x - 2t_p^\perp \cos k_y$ , and  $\epsilon_{p_{y\downarrow}}(\mathbf{k}) = \mu_p - m_z - 2t_p^\parallel \cos k_x - 2t_p^\parallel \cos k_y$  represent the energy bands for  $s_\uparrow$ ,  $p_{x\downarrow}$ , and  $p_{y\downarrow}$  states, respectively. It's worth noting that the  $\pi/a$ -momentum transfer between  $s_\uparrow$  and  $p_x(y)_\downarrow$  states effectively reverses the hopping coefficient  $t_p^\parallel \rightarrow -t_p^\parallel$  for the  $p_x(y)_\downarrow$  states, shifting the lowest energy points of  $\epsilon_{p_{x\downarrow}}$  ( $\epsilon_{p_{y\downarrow}}$ ) from  $\mathbf{Q}_x = (\pi, 0)$  ( $\mathbf{Q}_y = (0, \pi)$ ) to  $\mathbf{\Gamma} = (0, 0)$  [Fig.2 (a) and (b)]. Additionally, the energy spacing  $\epsilon_{s_\uparrow}(\mathbf{\Gamma}) - \epsilon_{p_x(y)_\downarrow}(\mathbf{\Gamma})$  can be tuned by the effective Zeeman splitting  $m_z$ . The remaining effect of spin-flipped hopping contributes to the SOC in the  $x - y$  plane, resulting in the four lowest energy points in the single-particle spectrum:  $\mathbf{k}_0^1 = (k_c, k_c)$ ,  $\mathbf{k}_0^2 = (-k_c, k_c)$ ,  $\mathbf{k}_0^3 = (-k_c, -k_c)$  and  $\mathbf{k}_0^4 = (k_c, -k_c)$ , which are connected by  $C_4$  symmetry [Fig.2 (c)].

## B.2 Interacting part

We next consider a contact potential  $V(\mathbf{r} - \mathbf{r}') = g_{\sigma\sigma'} \delta(\mathbf{r} - \mathbf{r}')$  ( $\sigma, \sigma' = \uparrow, \downarrow$ ), with the corresponding interaction Hamiltonian given by

$$\hat{H}_{\text{int}} = \frac{1}{2} \sum_{\sigma, \sigma'} \int d\mathbf{r} d\mathbf{r}' \Psi_\sigma^\dagger(\mathbf{r}) \Psi_{\sigma'}^\dagger(\mathbf{r}') V(\mathbf{r} - \mathbf{r}') \Psi_{\sigma'}(\mathbf{r}') \Psi_\sigma(\mathbf{r}), \tag{12}$$

where  $\Psi_\sigma^\dagger(\mathbf{r}) = \sum_{i,l} \phi_{i,\sigma}^*(\mathbf{r} - \mathbf{r}_i) b_{i,l,\sigma}^\dagger$  ( $l = s, p_x, p_y$ ;  $\sigma = \uparrow, \downarrow$ ). Here, only the single center integral terms in the above equation are retained

$$\hat{H}_{\text{int}} = \sum_{\sigma, \sigma'} \sum_{l_1, l_2, l_3, l_4} \sum_{\mathbf{i}} \frac{U_{l_1 l_2 l_3 l_4}^{\sigma\sigma'}}{2} b_{i,l_1,\sigma}^\dagger b_{i,l_2,\sigma'}^\dagger b_{i,l_3,\sigma'} b_{i,l_4,\sigma}, \tag{13}$$

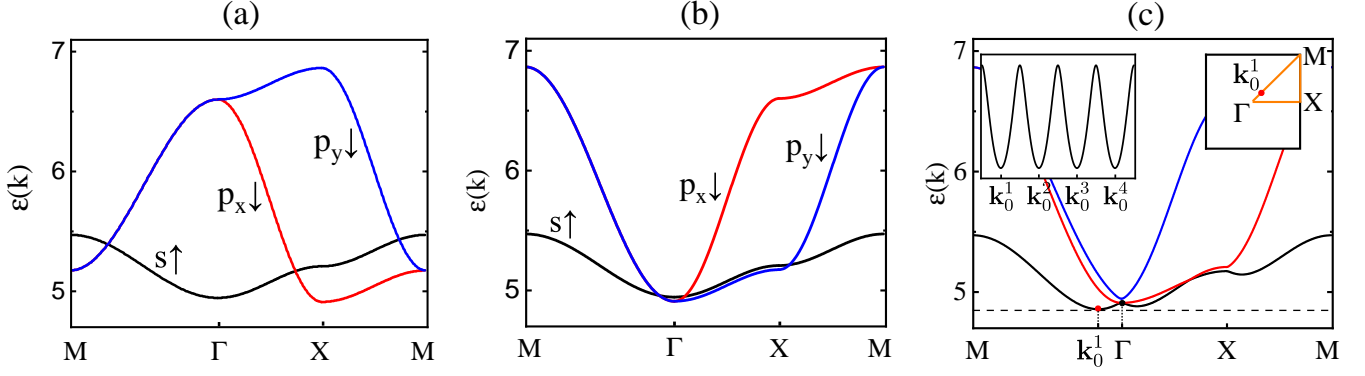


Figure 2: Single-particle spectrum. Here,  $V_0 = 5.0E_r$ ,  $M_0 = 1.0E_r$  (tight-binding parameters:  $t_s = 0.0658E_r$ ,  $t_p^\parallel = 0.4228E_r$ ,  $t_p^\perp = 0.0658E_r$ ,  $t_{so} = 0.1059E_r$ ,  $\mu_s = 5.1909E_r$ , and  $\mu_p = 5.9049E_r$ ),  $m_z = 0.0173E_r$ .  $E_r$  is the recoil energy. (a) and (b) demonstrate that the staggered properties of Raman-induced spin-flipped hoppings can result in a  $\pi/a$  momentum transfer for the  $p_x$  band and  $p_y$  band along the  $k_x$  and  $k_y$  directions, respectively. (c) shows the energy spectrum of the non-interacting Hamiltonian  $\mathcal{H}_0$ , which features the four lowest energy points related by  $C_4$  symmetry:  $\mathbf{k}_0^1, \mathbf{k}_0^2, \mathbf{k}_0^3, \mathbf{k}_0^4$ . Note that  $\mathbf{k}_0^1 = (0.154, 0.154)\pi$ .

with  $U_{l_1 l_2 l_3 l_4}^{\sigma\sigma'} = g_{\sigma\sigma'} \int d\mathbf{r} \phi_{l_1, \sigma}^*(\mathbf{r} - \mathbf{r}_i) \phi_{l_2, \sigma'}^*(\mathbf{r} - \mathbf{r}_i) \phi_{l_3, \sigma'}(\mathbf{r} - \mathbf{r}_i) \phi_{l_4, \sigma}(\mathbf{r} - \mathbf{r}_i)$ . Since we only focus on the orbital physics of the  $(s_\uparrow, p_{x\downarrow}, p_{y\downarrow})$  subspace, Eq.(13) can be reduced to

$$\begin{aligned} \hat{H}_{\text{int}} = & \frac{U_s}{2} \sum_i n_{i s_\uparrow} (n_{i s_\uparrow} - 1) + \frac{U_p}{2} \sum_{i\nu} n_{i p_{\nu\downarrow}} (n_{i p_{\nu\downarrow}} - 1) + U_{sp} \sum_i n_{i s_\uparrow} n_{i p_\downarrow} + 2\tilde{U}_p \sum_i n_{i p_{x\downarrow}} n_{i p_{y\downarrow}} \\ & + \frac{\tilde{U}_p}{2} \sum_i (b_{i p_{x\downarrow}}^\dagger b_{i p_{x\downarrow}}^\dagger b_{i p_{y\downarrow}} b_{i p_{y\downarrow}} + \text{H.c.}). \end{aligned} \quad (14)$$

Here,

$$\begin{aligned} U_s &= g \int d\mathbf{r} \phi_{s,\uparrow}^4(\mathbf{r} - \mathbf{r}_i), \\ U_{sp} &= g \int d\mathbf{r} \phi_{p_{\nu,\downarrow}}^2(\mathbf{r} - \mathbf{r}_i) \phi_{s,\uparrow}^2(\mathbf{r} - \mathbf{r}_i), \\ U_p &= g \int d\mathbf{r} \phi_{p_{\nu,\downarrow}}^4(\mathbf{r} - \mathbf{r}_i), \\ \tilde{U}_p &= g \int d\mathbf{r} \phi_{p_{\nu,\downarrow}}^2(\mathbf{r} - \mathbf{r}_i) \phi_{p_{\tilde{\nu},\downarrow}}^2(\mathbf{r} - \mathbf{r}_i), \quad \tilde{\nu} \neq \nu. \end{aligned} \quad (15)$$

Note that we take  $g_{\uparrow\uparrow} \approx g_{\uparrow\downarrow} \approx g_{\downarrow\downarrow} = g$ . In the harmonic approximation,  $\tilde{U}_p/U_p = 1/3$ , and Eq. (14) can be rewritten as

$$\hat{H}_{\text{int}} = \sum_i \left\{ \frac{U_s}{2} n_{i,s,\uparrow} (n_{i,s,\uparrow} - 1) + U_{sp} n_{i,s,\uparrow} n_{i,p,\downarrow} + \frac{U_p}{2} \left[ n_{i,p,\downarrow} (n_{i,p,\downarrow} - \frac{2}{3}) - \frac{1}{3} L_{i,z}^2 \right] \right\}, \quad (16)$$

where  $n_{i,p,\downarrow} = n_{i,p_{x,\downarrow}} + n_{i,p_{y,\downarrow}}$  and  $L_{i,z} = -ib_{i,p_{x,\downarrow}}^\dagger b_{i,p_{y,\downarrow}} + \text{H.c.}$ . Remarkably, the emergence of angular momentum order  $\langle L_{i,z} \rangle \neq 0$  will reduce the  $p$ -orbital interaction energy.

### B.3 Model parameters

Here we provide the appropriate model parameters

$$V_0 = 5.0E_r, \quad M_0 = 1.0E_r, \quad g = 0.01E_r. \quad (17)$$

For tight-binding Hamiltonian:  $t_s = 0.0658E_r$ ,  $t_p^\parallel = 0.4228E_r$ ,  $t_p^\perp = 0.0658E_r$ ,  $t_{so} = 0.1059E_r$ ,  $\mu_s = 5.1909E_r$ ,  $\mu_p = 5.9049E_r$ ,  $U_s = 0.1044E_r$ ,  $U_{sp} = 0.0428E_r$ ,  $U_p = 0.0618E_r$ ,  $\tilde{U}_p = 0.0175E_r$ . Moreover,  $m_z$  can be adjusted by two-photon detuning  $\delta$ , with  $m_z = 0.00E_r \sim 0.18E_r$ . Density of condensation bosons:  $N_0/N = 2 \sim 3$ .

## C Bogoliubov mean field theory

As presented in the main text, we discover two types of exotic condensed ground states of bosons: the uniform angular momentum superfluid phase and the two-dimensional spin-orbital supersolid phase, along with their respective non-trivial quasiparticle excitations. In this section, we will utilize the Bogoliubov-de Gennes (BdG) mean field theory to obtain the corresponding BdG Hamiltonian based on these two ground state phases.

### C.1 Uniform angular momentum superfluid phase

First, we derive the Bogoliubov excitation spectrum based on uniform angular momentum superfluid phase (UAMSF). We perform a Fourier transformation on the total Hamiltonian  $\hat{H} = \hat{H}_0 + \hat{H}_{\text{int}}$ , using  $b_{i,l,\sigma} = \frac{1}{\sqrt{N}} \sum_{\mathbf{k}} b_{\mathbf{k},l,\sigma} e^{i\mathbf{k}\cdot\mathbf{r}_i}$ . Consequently, the total Hamiltonian in momentum space is given by

$$\begin{aligned} \hat{\mathcal{H}} = & \sum_{\mathbf{k}} \left[ \epsilon_{s\uparrow}(\mathbf{k}) b_{\mathbf{k},s,\uparrow}^\dagger b_{\mathbf{k},s,\uparrow} + \epsilon_{p_x\downarrow}(\mathbf{k}) b_{\mathbf{k},p_x,\downarrow}^\dagger b_{\mathbf{k},p_x,\downarrow} + \epsilon_{p_y\downarrow}(\mathbf{k}) b_{\mathbf{k},p_y,\downarrow}^\dagger b_{\mathbf{k},p_y,\downarrow} \right. \\ & \left. - (2it_{so} \sin \mathbf{k}_x b_{\mathbf{k},s,\uparrow}^\dagger b_{\mathbf{k},p_x,\downarrow} + 2it_{so} \sin \mathbf{k}_y b_{\mathbf{k},s,\uparrow}^\dagger b_{\mathbf{k},p_y,\downarrow} + \text{H.c.}) \right] \\ & + \frac{1}{N} \sum_{\mathbf{k}_1+\mathbf{k}_2=\mathbf{k}_3+\mathbf{k}_4} \left[ \frac{U_s}{2} b_{\mathbf{k}_3,s,\uparrow}^\dagger b_{\mathbf{k}_4,s,\uparrow}^\dagger b_{\mathbf{k}_2,s,\uparrow} b_{\mathbf{k}_1,s,\uparrow} + U_{sp} \sum_{\nu=x,y} b_{\mathbf{k}_3,p_\nu,\downarrow}^\dagger b_{\mathbf{k}_4,s,\uparrow}^\dagger b_{\mathbf{k}_2,s,\uparrow} b_{\mathbf{k}_1,p_\nu,\downarrow} \right. \\ & + \frac{U_p}{2} \sum_{\nu=x,y} b_{\mathbf{k}_3,p_\nu,\downarrow}^\dagger b_{\mathbf{k}_4,p_\nu,\downarrow}^\dagger b_{\mathbf{k}_2,p_\nu,\downarrow} b_{\mathbf{k}_1,p_\nu,\downarrow} + 2\tilde{U}_p b_{\mathbf{k}_3,p_y,\downarrow}^\dagger b_{\mathbf{k}_4,p_x,\downarrow}^\dagger b_{\mathbf{k}_2,p_x,\downarrow} b_{\mathbf{k}_1,p_y,\downarrow} \\ & \left. + \frac{\tilde{U}_p}{2} (b_{\mathbf{k}_3,p_x,\downarrow}^\dagger b_{\mathbf{k}_4,p_x,\downarrow}^\dagger b_{\mathbf{k}_2,p_y,\downarrow} b_{\mathbf{k}_1,p_y,\downarrow} + b_{\mathbf{k}_3,p_y,\downarrow}^\dagger b_{\mathbf{k}_4,p_y,\downarrow}^\dagger b_{\mathbf{k}_2,p_x,\downarrow} b_{\mathbf{k}_1,p_x,\downarrow}) \right]. \end{aligned} \quad (18)$$

We have known that the ground-state wave function for the UAMSF takes the form

$$|G\rangle = e^{\sqrt{N_0}(\beta_{\Gamma,p_x\downarrow} b_{\Gamma,p_x,\downarrow}^\dagger + \beta_{\Gamma,p_y\downarrow} b_{\Gamma,p_y,\downarrow}^\dagger)} |\text{vac}\rangle, \quad \beta_{\Gamma,p_x\downarrow} = -i\beta_{\Gamma,p_y\downarrow}. \quad (19)$$

It is easy to see that

$$\langle G|b_{\mathbf{k},s,\uparrow}|G\rangle = 0, \quad \langle G|b_{\mathbf{k},p_x,\downarrow}|G\rangle = \beta_{\Gamma,p_x\downarrow} \sqrt{N_0} \delta_{\mathbf{k},\Gamma}, \quad \langle G|b_{\mathbf{k},p_y,\downarrow}|G\rangle = \beta_{\Gamma,p_y\downarrow} \sqrt{N_0} \delta_{\mathbf{k},\Gamma}. \quad (20)$$

Under the mean field approximation [1], we can obtain the BdG Hamiltonian  $\hat{\mathcal{H}}_{\text{BdG}} = \frac{1}{2} \sum_{\mathbf{k}} \Psi(\mathbf{k})^\dagger \mathcal{H}_{\text{BdG}}(\mathbf{k}) \Psi(\mathbf{k})$ , where the Nambu basis is chosen as  $\Psi(\mathbf{k}) = \left( b_{\mathbf{k},s,\uparrow} \quad b_{\mathbf{k},p_x,\downarrow} \quad b_{\mathbf{k},p_y,\downarrow} \quad b_{-\mathbf{k},s,\uparrow}^\dagger \quad b_{-\mathbf{k},p_x,\downarrow}^\dagger \quad b_{-\mathbf{k},p_y,\downarrow}^\dagger \right)^T$ , and the BdG Hamiltonian matrix reads

$$\mathcal{H}_{\text{BdG}}(\mathbf{k}) = \begin{pmatrix} h_0(\mathbf{k}) & h_{\text{int}}(\mathbf{k}) \\ h_{\text{int}}^\dagger(\mathbf{k}) & h_0^*(-\mathbf{k}) \end{pmatrix}. \quad (21)$$

Note that the diagonal element  $h_0(\mathbf{k}) = \mathcal{H}_0(\mathbf{k}) + \mathcal{H}'_{0,\text{int}} - \mu$ , where the first term takes the form of

$$\mathcal{H}_0(\mathbf{k}) = \begin{pmatrix} \epsilon_{s\uparrow}(\mathbf{k}) & -i2t_{so} \sin \mathbf{k}_x & -i2t_{so} \sin \mathbf{k}_y \\ i2t_{so} \sin \mathbf{k}_x & \epsilon_{p_x\downarrow}(\mathbf{k}) & 0 \\ i2t_{so} \sin \mathbf{k}_y & 0 & \epsilon_{p_y\downarrow}(\mathbf{k}) \end{pmatrix}, \quad (22)$$

and the second term reads  $\mathcal{H}'_{0,\text{int}} = \text{Diag}(h_{11}, h_{22}, h_{33})$  with  $h_{11} = 2U_{sp}n_0|\beta_{\Gamma,p_x\downarrow}|^2$ ,  $h_{22} = h_{33} = 2(U_p + \tilde{U}_p)n_0|\beta_{\Gamma,p_x\downarrow}|^2$ , and  $n_0 = \frac{N_0}{N}$ . Moreover, the third term  $\mu$  denotes the chemical potential. As for the off-diagonal element in Eq.(21),

$$h_{\text{int}}(\mathbf{k}) = n_0\beta_{\Gamma,p_x\downarrow}^2 \begin{pmatrix} 0 & 0 & 0 \\ 0 & U_p - \tilde{U}_p & i2\tilde{U}_p \\ 0 & i2\tilde{U}_p & \tilde{U}_p - U_p \end{pmatrix}. \quad (23)$$

Performing the Bogoliubov transformation, we have  $T_{\mathbf{k}}^\dagger \mathcal{H}_{\text{BdG}}(\mathbf{k}) T_{\mathbf{k}} = E_{\mathbf{k}}$ , where the para-unitary matrix  $T_{\mathbf{k}}$  satisfies  $T_{\mathbf{k}}^\dagger \tau_z T_{\mathbf{k}} = \tau_z$  ( $\tau_z = \sigma_z \otimes \mathbf{I}_{3 \times 3}$ ), and the diagonal terms of  $E_{\mathbf{k}}$  represent the excitation spectrum. Furthermore, the  $j^{\text{th}}$  column of  $T_{\mathbf{k}}$  denotes the eigenstate  $|T_{\mathbf{k}}^j\rangle$  of the  $j^{\text{th}}$  band. To investigate the topological properties of the excitation spectrum, we can calculate the corresponding topological invariant:

$$\mathbb{C}_j = \frac{1}{2\pi} \int d\mathbf{k} B_j(\mathbf{k}), \quad (24)$$

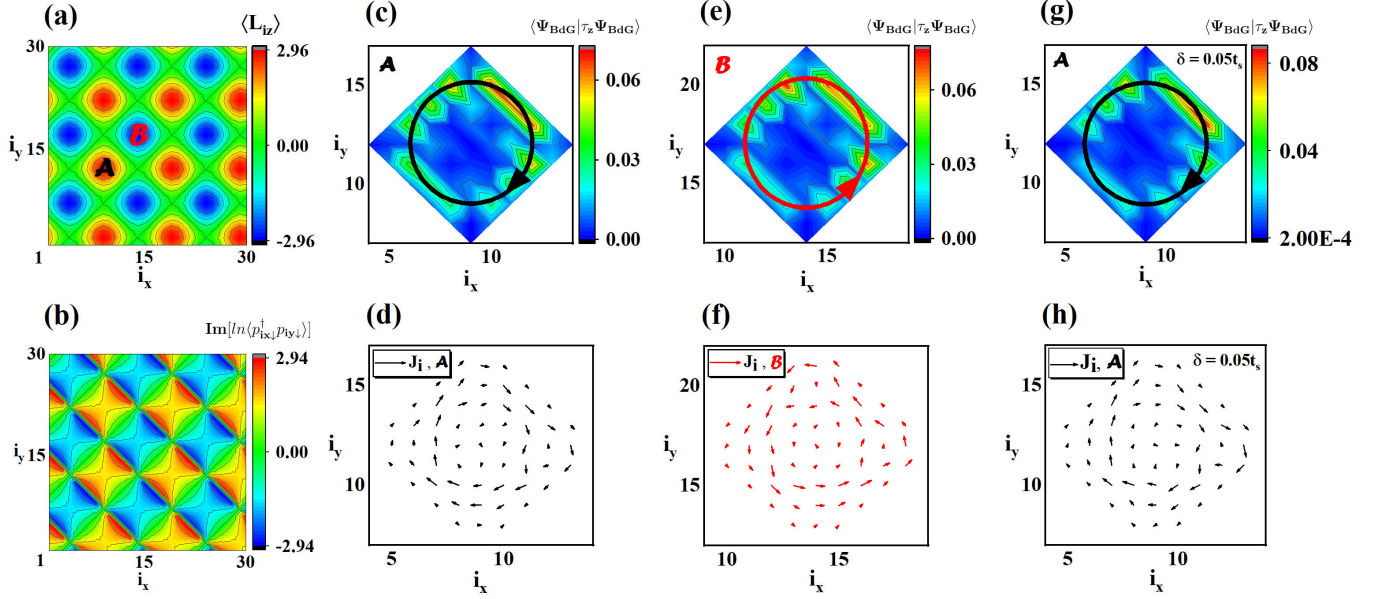


Figure 3: (a) Spatial pattern of orbital angular momentum order  $\langle L_{iz} \rangle$  for 2D SOSS. Here, we take the positive (A) and negative (B) clusters as examples to show the topological quasiparticle excitations on the cluster boundary. (b) Spatial distribution of the relative phase difference  $\theta_i = \text{Im}[\ln\langle b_{i,p_x,\downarrow}^\dagger b_{i,p_y,\downarrow} \rangle]$  between the  $p_x$  and  $p_y$  orbitals. There exist excited states that are distributed along the cluster boundary [(c) and (e)]. (d) and (f) show the expectation values of the current operators for the corresponding excited states, indicating that such boundary quasiparticle excitations of clusters A and B propagate clockwise and counterclockwise, respectively. Furthermore, we introduce the on-site random disorders with magnitude  $0.05t_s$  to the positive cluster A. As shown in (g) and (h), the edge excitation remains robust, manifesting that it is a topological boundary excitation. However, the topological boundary excitations at A and B have opposite chiralities, which results in the zero chiral current globally. In conclusion, the quasiparticle excitations for the 2D SOSS embody the properties of “topological in each cluster, trivial in the overall bulk”.

where the Berry curvature reads

$$B_j(\mathbf{k}) = \partial_{k_x} \mathcal{A}_y^j(\mathbf{k}) - \partial_{k_y} \mathcal{A}_x^j(\mathbf{k}), \quad (25)$$

and the Berry connection is given by

$$\mathcal{A}_\nu^j(\mathbf{k}) = -i \langle T_{\mathbf{k}}^j | \tau_z \partial_{k_\nu} | T_{\mathbf{k}}^j \rangle. \quad (26)$$

The Chern number of each band is shown in the Fig.3(b) in the main text.

## C.2 Two-dimensional spin-orbital supersolid phase

For the two-dimensional spin-orbital supersolid phase (SOSS), Bose-Einstein condensation (BEC) occurs equally at four momentum points  $\tilde{\mathbf{k}}_c^n$  ( $n = 1 \sim 4$ ), and the wave function for this ground state reads

$$|G\rangle = e^{\sqrt{N_0} \sum_n \gamma_{\tilde{\mathbf{k}}_c^n} (\beta_{\tilde{\mathbf{k}}_c^n, s_\uparrow} b_{\tilde{\mathbf{k}}_c^n, s_\uparrow}^\dagger + \beta_{\tilde{\mathbf{k}}_c^n, p_x \downarrow} b_{\tilde{\mathbf{k}}_c^n, p_x \downarrow}^\dagger + \beta_{\tilde{\mathbf{k}}_c^n, p_y \downarrow} b_{\tilde{\mathbf{k}}_c^n, p_y \downarrow}^\dagger + \beta_{\tilde{\mathbf{k}}_c^n, p_y \downarrow} b_{\tilde{\mathbf{k}}_c^n, p_y \downarrow}^\dagger)} | \text{vac} \rangle, \quad (27)$$

with parameters fulfilling  $|\gamma_{\tilde{\mathbf{k}}_c^n}|^2 = \frac{1}{4}$  and  $\beta_{\tilde{\mathbf{k}}_c^n, p_x \downarrow} = -(-1)^n \beta_{\tilde{\mathbf{k}}_c^n, p_y \downarrow}$ . As discussed in the main text, this ground state features a staggered pattern of positive and negative angular momentum clusters [Fig.3 (a)], resulting in zero net angular momentum in the real space. Here, we focus on a single angular momentum cluster to study its quasiparticle topological excitation. Since the lattice translational symmetry is broken within the angular momentum cluster, we can analyze the topological excitation in real space.

Similarly, the BEC order parameters for the ground state given in Eq.(27) are

$$\begin{aligned}
\langle G|b_{\mathbf{i},s,\uparrow}|G\rangle &= \sqrt{n_0} \sum_n \gamma_{\bar{\mathbf{k}}_c^n} \beta_{\bar{\mathbf{k}}_c^n, s\uparrow} e^{i\bar{\mathbf{k}}_c^n \cdot \mathbf{r}_i}, \\
\langle G|b_{\mathbf{i},p_x,\downarrow}|G\rangle &= \sqrt{n_0} \sum_n \gamma_{\bar{\mathbf{k}}_c^n} \beta_{\bar{\mathbf{k}}_c^n, p_x\downarrow} e^{i\bar{\mathbf{k}}_c^n \cdot \mathbf{r}_i}, \\
\langle G|b_{\mathbf{i},p_y,\downarrow}|G\rangle &= \sqrt{n_0} \sum_n \gamma_{\bar{\mathbf{k}}_c^n} \beta_{\bar{\mathbf{k}}_c^n, p_y\downarrow} e^{i\bar{\mathbf{k}}_c^n \cdot \mathbf{r}_i}.
\end{aligned} \tag{28}$$

With the Bogoliubov mean-field approximation, the BdG Hamiltonian in real space can be written as

$$\begin{aligned}
\hat{H}_{\text{BdG}} = \hat{H}_0 + n_0 \sum_{\mathbf{i}} \sum_{n_1, n_2} \left\{ [2U_s \beta_{s\uparrow}^{n_1*} \beta_{s\uparrow}^{n_2} + U_{sp} (\beta_{p_x\downarrow}^{n_1*} \beta_{p_x\downarrow}^{n_2} + \beta_{p_y\downarrow}^{n_1*} \beta_{p_y\downarrow}^{n_2})] \cdot e^{i \cdot (\bar{\mathbf{k}}_c^{n_2} - \bar{\mathbf{k}}_c^{n_1}) \cdot \mathbf{r}_i} b_{\mathbf{i},s,\uparrow}^\dagger b_{\mathbf{i},s,\uparrow} \right. \\
+ [2U_p \beta_{p_x\downarrow}^{n_1*} \beta_{p_x\downarrow}^{n_2} + 2\tilde{U}_p \beta_{p_y\downarrow}^{n_1*} \beta_{p_y\downarrow}^{n_2} + U_{sp} \beta_{s\uparrow}^{n_1*} \beta_{s\uparrow}^{n_2}] \cdot e^{i \cdot (\bar{\mathbf{k}}_c^{n_2} - \bar{\mathbf{k}}_c^{n_1}) \cdot \mathbf{r}_i} b_{\mathbf{i},p_x,\downarrow}^\dagger b_{\mathbf{i},p_x,\downarrow} \\
+ [2U_p \beta_{p_y\downarrow}^{n_1*} \beta_{p_y\downarrow}^{n_2} + 2\tilde{U}_p \beta_{p_x\downarrow}^{n_1*} \beta_{p_x\downarrow}^{n_2} + U_{sp} \beta_{s\uparrow}^{n_1*} \beta_{s\uparrow}^{n_2}] \cdot e^{i \cdot (\bar{\mathbf{k}}_c^{n_2} - \bar{\mathbf{k}}_c^{n_1}) \cdot \mathbf{r}_i} b_{\mathbf{i},p_y,\downarrow}^\dagger b_{\mathbf{i},p_y,\downarrow} \\
+ [(2\tilde{U}_p \beta_{p_x\downarrow}^{n_1*} \beta_{p_x\downarrow}^{n_2} + 2\tilde{U}_p \beta_{p_y\downarrow}^{n_1*} \beta_{p_y\downarrow}^{n_2}) \cdot e^{i \cdot (\bar{\mathbf{k}}_c^{n_2} - \bar{\mathbf{k}}_c^{n_1}) \cdot \mathbf{r}_i} b_{\mathbf{i},p_x,\downarrow}^\dagger b_{\mathbf{i},p_y,\downarrow} + \text{H.c.}] \\
+ [U_{sp} \beta_{s\uparrow}^{n_1*} \beta_{p_x\downarrow}^{n_2} \cdot e^{i \cdot (\bar{\mathbf{k}}_c^{n_2} - \bar{\mathbf{k}}_c^{n_1}) \cdot \mathbf{r}_i} b_{\mathbf{i},p_x,\downarrow}^\dagger b_{\mathbf{i},s,\uparrow} + U_{sp} \beta_{p_x\downarrow}^{n_1*} \beta_{s\uparrow}^{n_2} \cdot e^{i \cdot (\bar{\mathbf{k}}_c^{n_2} - \bar{\mathbf{k}}_c^{n_1}) \cdot \mathbf{r}_i} b_{\mathbf{i},s,\uparrow}^\dagger b_{\mathbf{i},p_x,\downarrow}] \\
+ [U_{sp} \beta_{s\uparrow}^{n_1*} \beta_{p_y\downarrow}^{n_2} \cdot e^{i \cdot (\bar{\mathbf{k}}_c^{n_2} - \bar{\mathbf{k}}_c^{n_1}) \cdot \mathbf{r}_i} b_{\mathbf{i},p_y,\downarrow}^\dagger b_{\mathbf{i},s,\uparrow} + \text{H.c.}] \\
+ [\frac{1}{2} U_s \beta_{s\uparrow}^{n_1*} \beta_{s\uparrow}^{n_2*} \cdot e^{-i \cdot (\bar{\mathbf{k}}_c^{n_2} + \bar{\mathbf{k}}_c^{n_1}) \cdot \mathbf{r}_i} b_{\mathbf{i},s,\uparrow} b_{\mathbf{i},s,\uparrow} + \text{H.c.}] \\
+ [\frac{1}{2} (U_p \beta_{p_x\downarrow}^{n_1*} \beta_{p_x\downarrow}^{n_2*} + \tilde{U}_p \beta_{p_y\downarrow}^{n_1*} \beta_{p_y\downarrow}^{n_2*}) \cdot e^{-i \cdot (\bar{\mathbf{k}}_c^{n_2} + \bar{\mathbf{k}}_c^{n_1}) \cdot \mathbf{r}_i} b_{\mathbf{i},p_x,\downarrow} b_{\mathbf{i},p_x,\downarrow} + \text{H.c.}] \\
+ [\frac{1}{2} (U_p \beta_{p_y\downarrow}^{n_1*} \beta_{p_y\downarrow}^{n_2*} + \tilde{U}_p \beta_{p_x\downarrow}^{n_1*} \beta_{p_x\downarrow}^{n_2*}) \cdot e^{-i \cdot (\bar{\mathbf{k}}_c^{n_2} + \bar{\mathbf{k}}_c^{n_1}) \cdot \mathbf{r}_i} b_{\mathbf{i},p_y,\downarrow} b_{\mathbf{i},p_y,\downarrow} + \text{H.c.}] \\
+ [2\tilde{U}_p \beta_{p_x\downarrow}^{n_1*} \beta_{p_y\downarrow}^{n_2*} \cdot e^{-i \cdot (\bar{\mathbf{k}}_c^{n_2} + \bar{\mathbf{k}}_c^{n_1}) \cdot \mathbf{r}_i} b_{\mathbf{i},p_x,\downarrow} b_{\mathbf{i},p_y,\downarrow} + \text{H.c.}] \\
+ [U_{sp} \beta_{p_x\downarrow}^{n_1*} \beta_{s\uparrow}^{n_2*} \cdot e^{-i \cdot (\bar{\mathbf{k}}_c^{n_2} + \bar{\mathbf{k}}_c^{n_1}) \cdot \mathbf{r}_i} b_{\mathbf{i},p_x,\downarrow} b_{\mathbf{i},s,\uparrow} + U_{sp} \beta_{s\uparrow}^{n_1} \beta_{p_x\downarrow}^{n_2} \cdot e^{i \cdot (\bar{\mathbf{k}}_c^{n_2} + \bar{\mathbf{k}}_c^{n_1}) \cdot \mathbf{r}_i} b_{\mathbf{i},s,\uparrow}^\dagger b_{\mathbf{i},p_x,\downarrow}^\dagger] \\
+ [U_{sp} \beta_{p_y\downarrow}^{n_1*} \beta_{s\uparrow}^{n_2*} \cdot e^{-i \cdot (\bar{\mathbf{k}}_c^{n_2} + \bar{\mathbf{k}}_c^{n_1}) \cdot \mathbf{r}_i} b_{\mathbf{i},p_y,\downarrow} b_{\mathbf{i},s,\uparrow} + \text{H.c.}] \left. \right\}, \tag{29}
\end{aligned}$$

where  $\beta_{l\sigma}^n \equiv \gamma_{\bar{\mathbf{k}}_c^n} \beta_{\bar{\mathbf{k}}_c^n, l\sigma}$ . Here, we focus on the angular momentum clusters A and B in Fig.3 (a) and solve the corresponding real space excitation spectrum to search for the excited states that primarily distribute on the cluster boundary and can withstand impurities or disorders (the essential properties of topological edge states). Calculating the expectation values of the current operators  $\hat{J}_i$  for the selected excited state, we find that there exists a chiral topological edge excitation [Fig.3 (c) and (e)] at each angular momentum cluster. Notably, the positive (A) and negative (B) clusters exhibit edge excitation with opposite chiralities [Fig.3 (d) and (f)].

## D Lifetime of the exotic many-body ground states

The uniform angular momentum superfluid phase and the two-dimensional spin-orbital supersolid phase are indeed metastable states due to the  $p$ -band population of bosons. Usually, the  $p$ -orbital bosons are unstable and will decay under interaction, even if weak. For spinless cases, an elastic decaying process that conserves total energy involves two bosons initially in the  $p$  band scattering into the final state where one boson is in the  $s$  band and the other in the  $d$  band [Fig.4 (a)]. Currently, the ‘‘double-well’’ lattice scheme can effectively extend the lifetime of the  $p$ -orbital bosons. As shown in Fig.4 (b), the ‘‘double-well’’ lattice consists of a deep well and a shallow well, with the  $p$  orbital of the deep well close to  $s$  orbital of the shallow well. Since the bosons can tunnel from the  $p$  orbital of a deep well to the  $s$  orbital of the nearest neighboring shallow well, and the  $s$  orbitals of the two wells have almost no overlap, the  $s$ -orbital bosons in the shallow well do not decay like the  $p$ -orbital one of deep well [2]. This results in a quite stable high-orbital many-body state. Notably, the present orbital optical Raman lattice scheme plays a similar role in extending the lifetime as the sublattice degrees of freedom in the ‘‘double-well’’ lattice are replaced by spin degrees of freedom in the orbital optical Raman lattice. Although two  $p_\downarrow$ -orbital bosons can scatter into an  $s_\downarrow$ -orbital boson and a  $d_\downarrow$ -orbital boson, the Raman-induced nearest neighbor  $p_\downarrow$ - $s_\uparrow$  transition leads to the population of  $s_\uparrow$ -orbital bosons. As shown in Fig.4 (c), these  $s_\uparrow$ -orbital bosons do not decay like the  $p_\downarrow$ -orbital ones due to the conservation of spin under interaction, making the high-orbital many-body states remain stable.

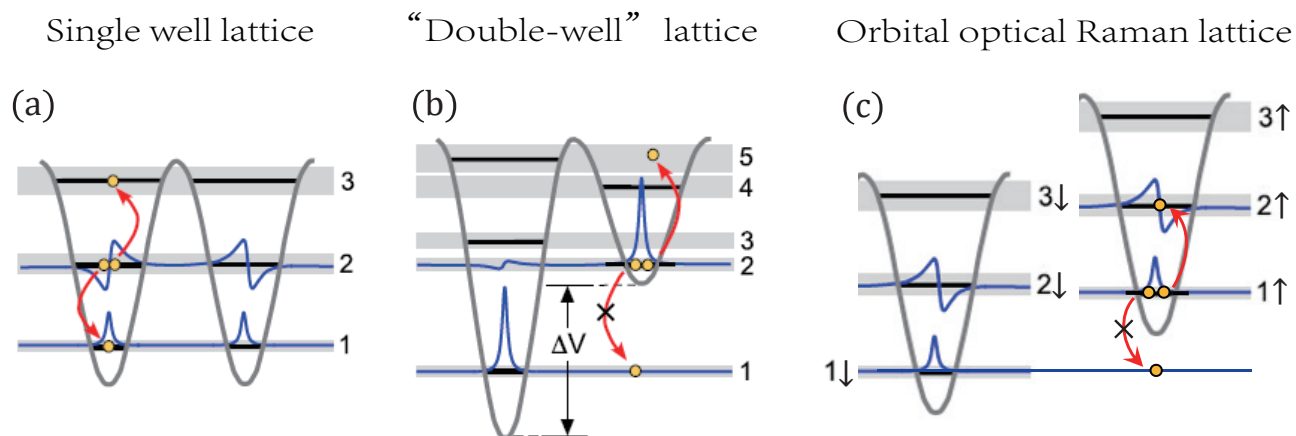


Figure 4: The similarity between the “double-well” lattice and the orbital optical Raman lattice in prolonging the lifetime of  $p$ -orbital bosons. Here, Fig.(a) and (b) are taken from Ref.[2]. (a). The  $p$ -orbital bosons are usually unstable and will soon decay through an elastic scattering process  $(p, p) \Rightarrow (s, d)$  within a single well. (b). In the “double-well” lattice, the  $s$ -orbital of the shallow well is close to the  $p$ -orbital of the deep well. As demonstrated in Ref.[2], such a configuration can be tuned to clearly slow down the decay of the boson population in the mixed  $s$ -orbital in the shallow well and  $p$ -orbital in the deep well, but appreciable decay can still proceed according to the elastic scattering process shown in (a). (c). In the orbital optical Raman lattice, Raman coupling can effectively bring the  $s_{\uparrow}$  and  $p_{\downarrow}$  orbitals closer together and facilitate the nearest-neighbor  $p_{\downarrow}$ - $s_{\uparrow}$  hopping. This causes bosons to populate the  $s_{\uparrow}$ -orbital, thereby further substantially suppressing the decay process  $(p_{\downarrow}, p_{\downarrow}) \Rightarrow (s_{\downarrow}, d_{\downarrow})$  compared with the already successful step in (b).

## References

- [1] Hui Zhai. *Ultracold atomic physics*, chapter 3, pages 88–89. Cambridge University Press, 2021.
- [2] T Kock, C Hippler, A Ewerbeck, and A Hemmerich. Orbital optical lattices with bosons. *Journal of Physics B: Atomic, Molecular and Optical Physics*, 49(4):042001, 2016.